ACS OMEGA

http://pubs.acs.org/journal/acsodf

Article

# Efficient Visible-Light Photocatalysis and Antibacterial Activity of $TiO_2$-$Fe_3C$-Fe-$Fe_3O_4$/Graphitic Carbon Composites Fabricated by Catalytic Graphitization of Sucrose Using Natural Ilmenite

Charitha Thambiliyagodage,* Leshan Usgodaarachchi, Madara Jayanetti, Chamika Liyanaarachchi, Murthi Kandanapitiye, and Saravanamuthu Vigneswaran

Cite This: *ACS Omega* 2022, 7, 25403−25421

Read Online

ACCESS | Metrics & More | Article Recommendations | Supporting Information

**ABSTRACT:** Dyes in wastewater are a serious problem that needs to be resolved. Adsorption coupled photocatalysis is an innovative technique used to remove dyes from contaminated water. Novel composites of $TiO_2$-$Fe_3C$-Fe-$Fe_3O_4$ dispersed on graphitic carbon were fabricated using natural ilmenite sand as the source of iron and titanium, and sucrose as the carbon source, which were available at no cost. Synthesized composites were characterized by X-ray diffractometry (XRD), Raman spectroscopy, transmission electron microscopy (TEM), scanning electron microscopy (SEM), X-ray photoelectron spectroscopy (XPS), X-ray fluorescence spectroscopy (XRF), and diffuse reflectance UV−visible spectroscopy (DRS). Arrangement of nanoribbons of graphitic carbon with respect to the nanomaterials was observed in TEM images, revealing the occurrence of catalytic graphitization. Variations in the intensity ratio $(I_D/I_G)$, $L_a$ and $L_D$, calculated from data obtained from Raman spectroscopy suggested that the level of graphitization increased with an increased loading of the catalysts. SEM images show the immobilization of nanoplate microballs and nanoparticles on the graphitic carbon matrix. The catalyst surface consists of $Fe^{3+}$ and $Ti^{4+}$ as the metal species, with V, Mn, and Zr being the main impurities. According to DRS spectra, the synthesized composites absorb light in the visible region efficiently. Fabricated composites effectively adsorb methylene blue via $\pi-\pi$ interactions, with the absorption capacities ranging from 21.18 to 45.87 mg/g. They were effective in photodegrading methylene blue under sunlight, where the rate constants varied in the 0.003−0.007 $min^{-1}$ range. Photogenerated electrons produced by photocatalysts captured by graphitic carbon produce $O_2^{\bullet-}$ radicals, while holes generate $OH^{\bullet}$ radicals, which effectively degrade methylene blue molecules. $TiO_2$-$Fe_3C$-Fe-$Fe_3O_4$/graphitic carbon composites inhibited the growth of *Escherichia coli* (69%) and *Staphylococcus aureus* (92%) under visible light. Synthesized novel composites using natural materials comprise an ecofriendly, cost-effective solution to remove dyes, and they were effective in inhibiting the growth of Gram-negative and Gram-positive bacteria.

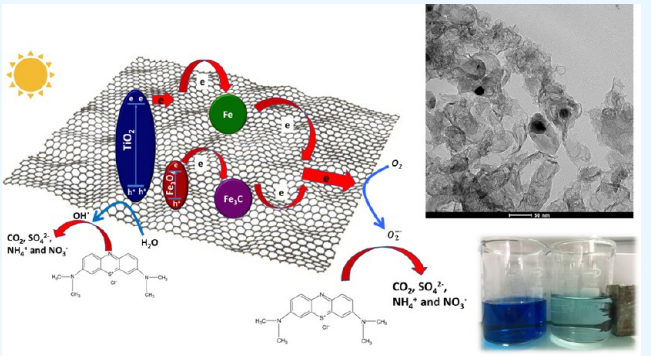


## 1. INTRODUCTION

Graphite is the most thermodynamically stable allotrope of carbon among graphite, diamond, and fullerenes. It has garnered more attention due to its physicochemical properties including chemical and thermal stability, high lubricity, thermal and electrical conductivity, and electrochemical lithium storage.[1−5] Graphite either needs to be separated from natural graphite or synthesized by carbon precursors, where the latter path is achieved by either direct graphitization or catalytic graphitization. Graphitization is the solid-state transformation of non-graphitic carbon to graphitic carbon with the aid of high temperatures. Direct graphitization of graphitizable carbon involves high temperatures, for example, ∼3000 °C, while catalytic graphitization of nongraphitizable carbon requires a moderate temperature of ∼1000 °C. Catalytic graphitization is preferred by the industry, which demands a graphitic carbon since it is economically viable due to the required low temperatures.[6,7]

Carbon precursors such as furfuryl alcohol,[8] phenolic resins,[9] polymer spheres,[10] and amorphous carbon films[11] have been employed. Recently, biomass, including sucrose,[12] cellulose,[13] and sawdust,[13] has emerged as a cheap precursor. Various metals, including Fe, Co, Ni, Cr, Mn, and Ti, have served as catalysts for the graphitization process.[13−15] In this study, we were interested in assessing the use of sucrose as the carbon

Received: April 14, 2022
Accepted: July 6, 2022
Published: July 15, 2022

precursor and naturally available ilmenite as the raw material for the catalyst of graphitization and their effectiveness in purifying water. Ilmenite is found on beaches and hard rock deposits in countries including Australia, the USA, Brazil, India, Vietnam, and Sri Lanka, where their composition varies qualitatively and quantitatively. Different solutions are used to extract titanium and iron from ilmenite such as hydrochloric acid, sulfuric acid, potassium hydroxide, and ammonium chloride.[16] Furthermore, preliminary techniques like ball-milling can enhance the dissolution in the above solvents.[17] Ilmenite sand has not been used widely, except to produce $TiO_2$ as the white color pigment and to fabricate novel photocatalysts including $Fe_2TiO_5/TiO_2$[18] and $Fe_2O_3/Fe_2TiO_5/TiO_2$.[19] Therefore, adding value to ilmenite sand is of great importance. According to our current knowledge, using ilmenite as the source of catalyst for graphitization has not been reported previously.

Water decontamination has achieved global momentum due to increasing water scarcity, which is the result of water pollution caused by anthropogenic activities. Pollutants, including dyes,[20] pesticides,[21] fertilizers,[22] heavy metals,[23] and pharmaceuticals,[24] are released to normal water reservoirs due to the processes of industrialization. Among such pollutants, dyes that are released as part of water effluents from industries like paint, textiles, paper, cosmetics, leather, and plastics are endangering the health of humans, flora, and fauna.[20,25] Dyes remain stable in different environmental conditions and can resist biodegradation due to their synthetic nature.[26] They cause changes in chemical oxygen demand, biological oxygen demand, and the pH of water,[27] while the color affects the aesthetic value.[28] Moreover, the presence of dyes restricts the ability of light to penetrate water bodies, subsequently limiting photosynthesis by aquatic living beings.[29] Additionally, with the release of dyes, other chemicals such as heavy metals, chlorinated compounds, surfactants, and salts are discharged.[30] For this reason, it is important to remove dyes from water reservoirs, and for such purposes, different methods including adsorption,[31−33] membrane filtration,[34] ion exchange,[35] coagulation,[36] and advanced oxidation process[18,19,37] are available.

Individually considered adsorption and advanced oxidation processes have both been researched, yet they do have certain disadvantages. The main problem of using adsorption to remove dyes is the ultimate destiny of pollutants. Despite the fact that dyes are removed from wastewater, they are deposited on an adsorbent and hence the pollutant simply ends up somewhere else. Advanced oxidation processes have been widely applied for $H_2$ production[38,39] and pollutant degradation in wastewater.[40,41] However, the main drawback of this process is the poor visible-light sensitivity and the electron−hole pair recombination, which leads to low photocatalytic activity. It should be noted that both processes have more advantages rather than disadvantages. Once both techniques are combined, the above-mentioned disadvantages are eliminated because the dyes adsorbed to the adsorbents are degraded easily by photocatalysts immobilized on these adsorbents. Furthermore, the electrons excited to the conduction band are taken by the adsorbents and subjected to radical formation, thus elevating the charge separation and leading to higher photocatalytic activity. Pollutants have been removed by adsorption, photocatalysis, and adsorption coupled photocatalysis using various composites decorated with carbon-based materials including $TiO_2$/activated carbon,[42] $TiO_2$/carbon nanotubes,[43] $TiO_2$-reduced graphene oxide,[44] ZnO-reduced graphene oxide-carbon nanotubes,[45,46] and ethylene glycol capped ZnO.[47]

Graphene-based adsorbents have been used to adsorb heavy metals[48] and dyes.[12] Composites enriched with graphitic carbon have not been popularly studied for dye adsorption, photocatalysis, and solar cells[44,49,50] although g-$C_3N_4$ has been coupled to many materials widely researched such as $Ce^{3+}$/g-$C_3N_4$,[51] BiOI sheet-stacked g-$C_3N_4$,[52] and P-doped $MoS_2$/g-$C_3N_4$.[53] Subsequently, we became interested in fabricating graphitic carbon-based new composites consisting of $TiO_2$, $Fe_3C$, Fe, and $Fe_3O_4$ nanoparticles using natural ilmenite sand and sucrose as the raw materials to remove and degrade methylene blue in the water. Dye removal is a critical problem that needs to be addressed by the industrial sector. Further, the accumulation of Gram-negative and Gram-positive bacteria causes severe health issues. Fabrication of the new photocatalysts using ilmenite is a value addition to the raw material. Sucrose is a low-cost carbon-rich material. Hence, reported here in this study is an environmentally friendly, cost-effective solution to remove dyes and bacteria from industrial wastewater.

## 2. MATERIALS AND METHODS

**2.1. Materials.** Ilmenite was supplied by Lanka Mineral Sands Ltd. HCl (35%), $NH_3$ (25%), and NaOH were procured from Fisher Scientific. $FeCl_3$ was purchased from Sisco Research Laboratories (Pvt) Ltd, India. Methylene blue was sourced from Daejung Chemical & Metal Co., Ltd. $AgNO_3$ (99%) was supplied by Himedia Leading Biosciences Company. All chemicals used in the experiment were of analytical grade and used without further purification. Deionized water (DI), with resistivity greater than 18.0 MΩ.cm (Millipore Milli-Q system), was used in all experiments.

**2.2. Preparation of Nanomaterials.** *2.2.1. Synthesis of $\alpha$-$Fe_2O_3$.* A simple coprecipitation method was employed. NaOH solution (1.878 mol/dm$^3$, 100 mL) was added dropwise to 100 mL of 0.626 mol/dm$^3$ $FeCl_3$ solution while stirring, and the obtained brown-color precipitate was washed with deionized water. This was followed by drying in an oven at 80 °C for 6 h. The dried product was then annealed at 800 °C for 2 h.

*2.2.2. Synthesis of $Fe_2TiO_5/TiO_2$.* Ilmenite sand was washed with deionized water several times and dried before use. Ilmenite sand (12 g) was digested in 200 mL of 35% HCl at 90 °C for 6 h under refluxing and subjected to stirring, which continued overnight. The resulting leachate was pipetted out, and another 200 mL of 35% HCl was added to the remaining ilmenite sand, and refluxing was continued utilizing the above procedure. The leaching procedure was repeated twice with 100 mL of HCl. All of the leachates were combined, and 25% $NH_3$ was added dropwise until the pH of the solution reached 10. The obtained brown-color precipitate was washed with an abundant volume of deionized water until the washings were negative for the chloride test ($AgNO_3$ test) and the pH reached a neutral value. The precipitate was dried at 80 °C and denoted as fluorine-doped tin oxide (FTO) in the text.

*2.2.3. Synthesis of Amorphous Carbon.* Sucrose was dissolved in a minimum volume of deionized water, and the solution was heated while stirring until the sugar became caramelized. Then, the obtained product was ground and pyrolyzed in a tube furnace at 800 °C for 2 h in a $N_2$ atmosphere. The obtained amorphous carbon product is denoted as (S) in the text.

*2.2.4. Synthesis of SF Composites.* Sucrose was dissolved in a minimum volume of deionized water, and $\alpha$-$Fe_2O_3$ powder was added to the stirring solution in different weight ratios to the weight of sucrose as follows: sucrose/$\alpha$-$Fe_2O_3$, 10:1, 5:1, 2.5:1,


https://doi.org/10.1021/acsomega.2c02336
ACS Omega 2022, 7, 25403−25421

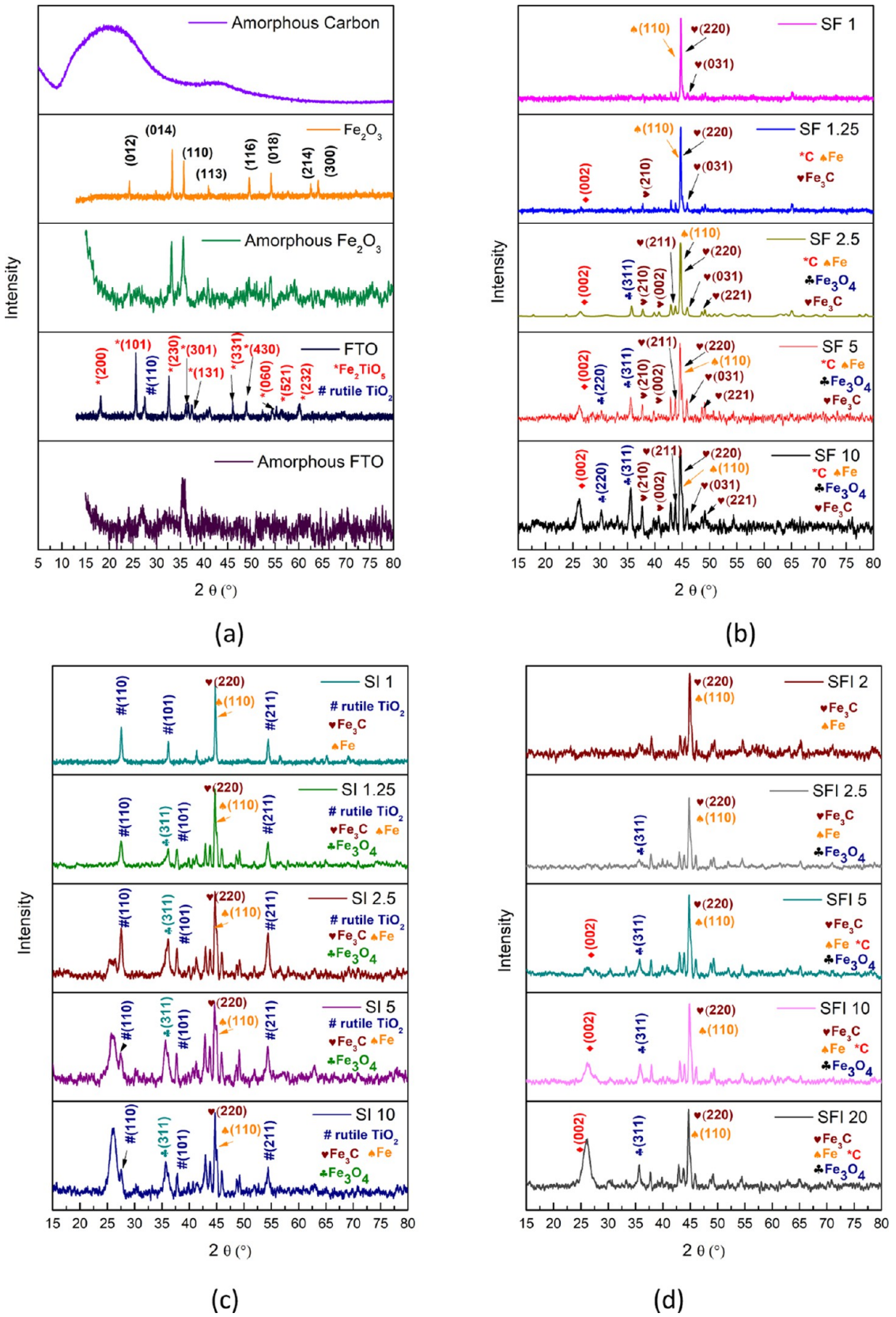


**Figure 1.** XRD patterns of (a) precursor compounds, (b) SF composites, (c) SI composites, and (d) SFI composites.

1.25:1, and 1:1 and they are abbreviated in the text as SF 10, SF 5, SF 2.5, SF 1.25, and SF 1, respectively. The mixture was stirred for 2 h and heated until the sugar became caramelized. The obtained solid was ground and pyrolyzed in a tube furnace at 800 °C for 2 h in a $N_2$ atmosphere.

*2.2.5. Synthesis of SI Composites.* The synthesis procedure was the same as that documented in section 2.2.4, except that



https://doi.org/10.1021/acsomega.2c02336
ACS Omega 2022, 7, 25403−25421

instead of $\alpha$-$Fe_2O_3$ powder, FTO powder was used in the same weight ratios. They are abbreviated as SI 10, SI 5, SI 2.5, SI 1.25, and SI 1, respectively.

*2.2.6. Synthesis of SFI Composites.* The synthesis procedure was the same as that reported in section 2.2.4, except that instead of $\alpha$-$Fe_2O_3$ powder, a mixture of $\alpha$-$Fe_2O_3$ and FTO powder was added to sucrose as follows: sucrose/$\alpha$-$Fe_2O_3$/FTO, 20:1:1, 10:1:1, 5:1:1, 2.5:1:1, and 2:1:1, where the sucrose-to-total-metal-oxide ratios were maintained as stated in section 2.4 (10:1, 5:1, 2.5:1, 1.25:1, and 1:1). They are denoted as SFI 20, SFI 10, SFI 5, SFI 2.5, and SFI 2, respectively.

**2.3. Antibacterial Activity.** *2.3.1. Microbial Strain and Inoculum Preparation.* The test organisms *E. coli* and *Staphylococcus aureus* were procured from Medical Research Institute, Sri Lanka. For preparing the inoculum, *E. coli* and *S. aureus* were cultured in a nutrient broth at 37 °C overnight. The microbial cultures were subcultured before the assay and later diluted to obtain a microbial suspension of $5 \times 10^5$ colony-forming units (CFUs)/mL for further analysis.

*2.3.2. Broth Dilution Assay.* The antibacterial activity of SI 10 and SFI 20 composites was investigated using the broth dilution method. The antibacterial effect of SI 10 and SFI 20 composites was tested against *E. coli* and *S. aureus* in a sterilized nutrient broth medium.

For the broth dilution assay, a 24 h aged bacterial culture was adjusted to obtain $5 \times 10^5$ CFU/mL with a 0.5 McFarland turbidity standard as the visual yardstick and a spectrophotometer. The adjusted bacterial suspension was used within 30 min to avoid changes in the cell count. Nanoparticle suspensions were prepared by sonicating the synthesized nanoparticles in deionized water for 1 h. The freshly prepared overnight culture (1 mL) was inoculated to 5 mL of sterilized nutrient broth medium containing 1 mL of 100 mg/mL composite suspensions. Additionally, 1 mL of the bacterial culture was inoculated to 5 mL of the sterilized nutrient broth medium containing 1 mL of Amoxicillin (100 mg/mL) as a positive control. The nanocomposite-free broth medium inoculated with both bacterial cultures served as the growth control. The nutrient broth medium with nanocomposites alone was retained as the blank. All tubes were incubated in a temperature-controlled shaker (150 drpm) at 30°C overnight for 24 h. After the incubation, optical density (OD) was recorded at 600 nm to measure the turbidity and, subsequently, inhibition of growth was determined. All experiments were done in triplicate. Three values of OD for each sample and their mean were calculated with standard deviation.

Percentage inhibition of growth was calculated using the following formula

$$\%\ \text{inhibition} = \frac{(\text{OD})_{\text{control}} - (\text{OD})_{\text{test}}}{(\text{OD})_{\text{control}}}$$

where (OD) control is the absorbance of the control sample and (OD) test is the absorbance of the test sample with the composites

## 3. CHARACTERIZATION

XRD patterns were collected via the D8 Advance Bruker system using Cu K$\alpha$ ($\lambda$ = 0.154 nm) radiation varying the 2$\theta$ from 5 to 80° at a scan speed of 2 °/min. The morphology of the synthesized nanocomposites was characterized by transmission electron microscopy (TEM). The microscope was operated at 200 kV (JEOL—JEM-2100), and energy-dispersive spectra (EDS) were collected by the same instrument with TEAM EDX software. The sample (1 $\mu$L) was mounted on a carbon copper grid with holes and allowed to dry at room temperature prior to TEM analysis. Scanning electron microscopic (SEM) images were acquired utilizing a Carl ZEISS EVO 18 RESEARCH instrument, while the EDX spectra were collected with the EDAX element EDS system. The samples' chemical compositions were analyzed by X-ray fluorescence (XRF) using a HORIBA Scientific XGT-5200 X-ray analytical microscope, equipped with a Rh anode X-ray tube operated at a maximum voltage of 50 kV. The survey spectra and the higher-resolution spectra of the synthesized catalysts were acquired by the Thermo Scientific ESCALAB $Xi^+$ X-ray photoelectron spectrometer. The Shimadzu 1800 UV−visible spectrophotometer utilizing a precision Czerny−Turner optical system served to collect diffuse reflectance spectra of the prepared powder samples. Measurements were carried out through the 400 to 750 nm range with a bandwidth of 1.0 nm (wavelength accuracy ±0.1 nm). Raman analysis was done using a Bruker Senterra Raman microscope spectrophotometer. The absorbance of MB samples was measured by a Shimadzu UV-1990 double-beam UV−visible spectrophotometer.

## 4. RESULTS AND DISCUSSION

**4.1. XRD Analysis.** X-ray diffraction patterns were gathered to understand the crystal nature of the synthesized composites. XRD patterns of the precursor compounds synthesized are depicted in Figure 1a. The XRD pattern of the FTO shows broad peaks at 27.5 and 36.5°, which correspond to the (110) and (101) of the rutile phase. However, other peaks could not be differentiated due to the low signal-to-noise ratio. The pattern indicates the amorphous nature of the synthesized materials, for which the degree of crystallinity is very low. Upon annealing at 800 °C for 2 h, the crystallinity of the materials improved and sharp peaks, which could be easily differentiated, were observed. XRD patterns of FTO show peaks at 2$\theta$, 18.08, 25.54, 32.52, 36.54, 37.34, 40.58, 41.06, 46.06, 48.86, 55.10, 56.20, and 60.06°. These could be indexed, respectively, to the (200), (101), (230), (301), (131), (240), (420), (331), (430), (060), (521), and (232) planes of the orthorhombic phase of $Fe_2TiO_5$ (pseudobrookite) (JCPDS card No: 41-1432). The calculated d-spacings of 0.490, 0.349, 0.275, 0.248, 0.222, 0.219, 0.197, 0.187, 0.166, and 0.154 nm agreed well with the ICSD reference ($a_o$ = 9.779 Å, $b_0$ = 9.978 Å, $c_0$ = 3.739 Å). Other peaks at 27.40° ($d$ = 0.325 nm) and 54.32° (0.168 nm) could be attributed to the (110) and (211) planes of the rutile phase.

The XRD pattern of amorphous $Fe_2O_3$ shows peaks at 33.40 and 35.86°, which correspond to the (104) and (110) planes. Upon annealing, the crystal structure of $\alpha$-$Fe_2O_3$ was established. The pattern consisted of peaks at 24.42, 33.40, 35.86, 41.12, 49.68, 54.32, 57.86, 62.64, and 64.26° corresponding to the (012), (104), (110), (113), (024), (116), (018), (214), and (300) planes of $\alpha$-$Fe_2O_3$ (JCPDS card No: 79-0007). Calculated lattice parameters a (5.016 Å) and c (13.626 Å) and the unit cell volume (296.90 $Å^3$) are consistent with the values reported for the hexagonal $\alpha$-$Fe_2O_3$ in the literature.[54] The broad peak centered at 22° in the XRD pattern of carbon confirms the presence of amorphous carbon.

XRD patterns of the SF composites are exhibited in Figure 1b. The peak at 26.5° corresponds to the (002) plane of graphitic carbon with a d-spacing of 0.3480 nm, suggesting the formation of turbostratic carbon, and furthermore, the d-spacing value did not change with the increased loading of $\alpha$-$Fe_2O_3$. Peaks at 30.2


https://doi.org/10.1021/acsomega.2c02336
ACS Omega 2022, 7, 25403−25421

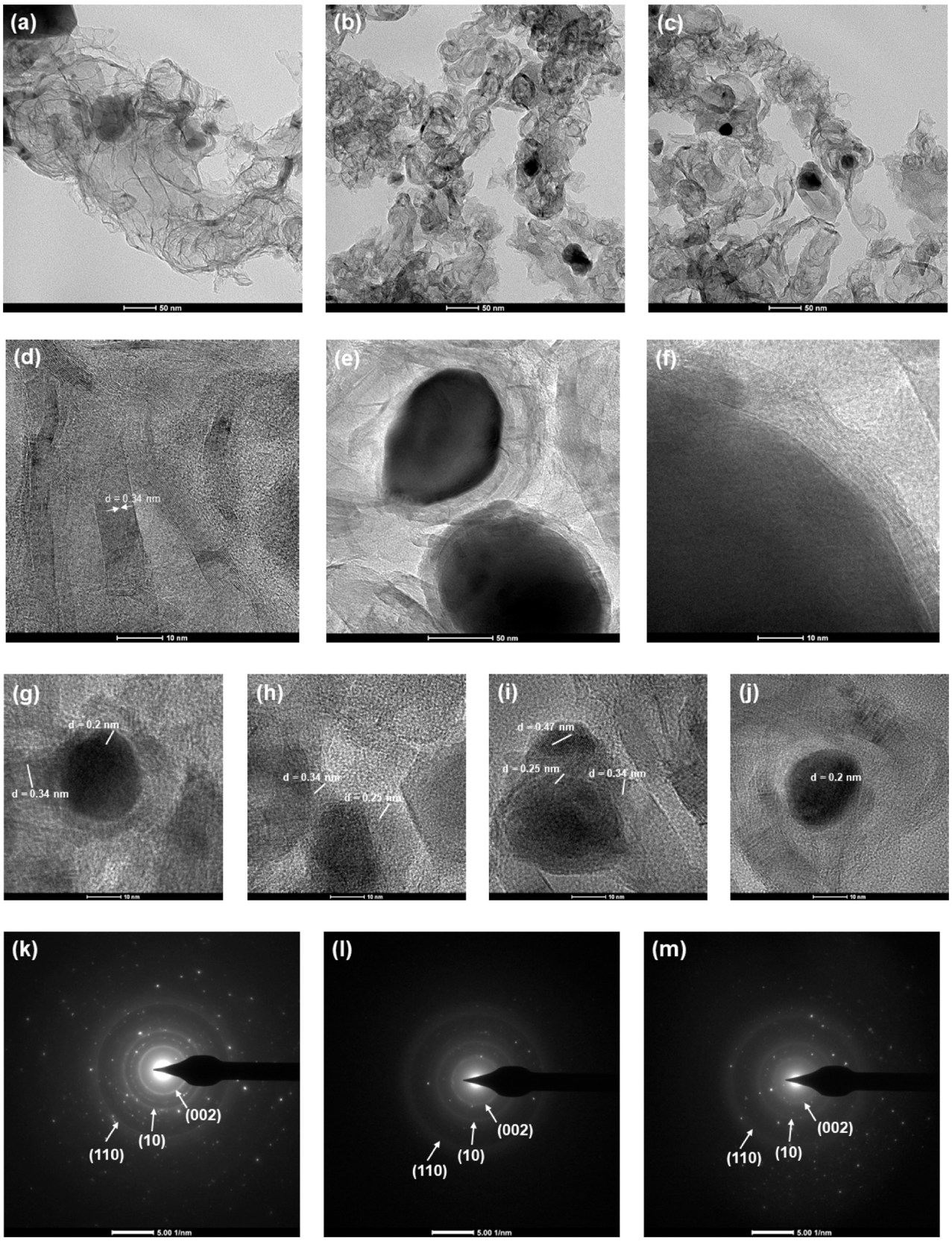


**Figure 2.** Bright-field TEM images of (a) SF 10, (b) SI 10, and (c) SFI 20. HRTEM images of (d) SI 10, (e) and (f) SF 2.5, (g) SI 10, and (h), (i), and (j) SFI 20. Selected area diffraction patterns of (k) SF 2.5, (l) SI 10, and (m) SFI 20.

and 35.6° are attributed to the (220) and (311) planes of $Fe_3O_4$. The interlayer spacing of $Fe_3O_4$ calculated using the peak at 35.6° is 0.2517 nm, and the crystallite size calculated using the peak is 39.4 nm. Peaks at 37.7, 39.9, 40.7, 42.9, 43.8, 44.6, 45.1, 48.6, and 49.2° correspond to the (210), (002), (201), (211), (102), (220), (031), (131) and (221) planes of $Fe_3C$ (JCPDS



https://doi.org/10.1021/acsomega.2c02336
ACS Omega 2022, 7, 25403−25421

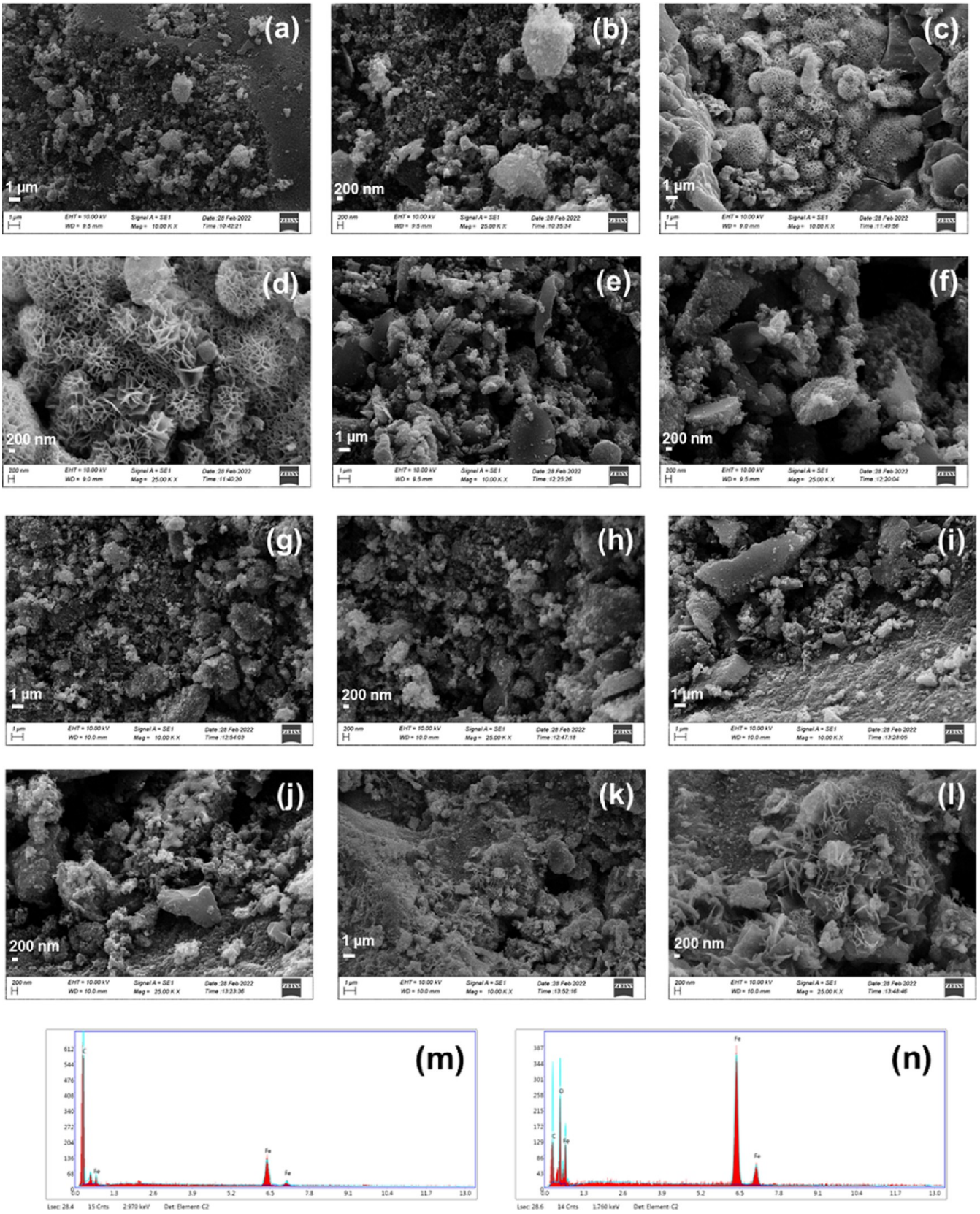


**Figure 3.** continued



https://doi.org/10.1021/acsomega.2c02336
*ACS Omega* 2022, 7, 25403−25421

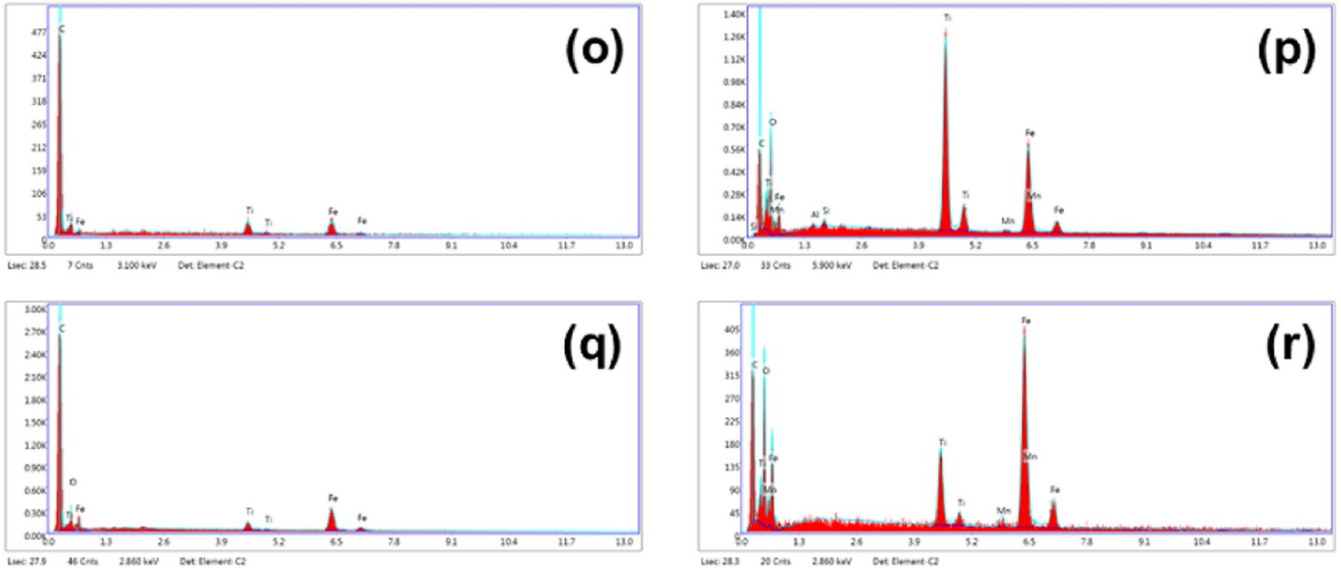


**Figure 3.** SEM images of (a), (b) SF 10 (c), (d) SF 1 (e), (f) SI 10 (g), (h) SI 1 (i), (j) SFI 20 (k), (l) SFI 2, EDX spectra of (m) SF 10 (n) SF 1 (o) SI 10 (p) SI 1 (q) SFI 20 (r) SFI 2.

card No: 89-2867). The d-spacing calculated using the highest intensity peak at 44.6° is 0.2027 nm, while the calculated crystallite size is 82.7 nm. The peak at 44.6° is attributable to the (110) plane of bcc Fe (0) because the peak at 65.0° is attributed to the (110) plane of Fe (0). The peak corresponding to graphitic carbon decreased with an increased loading of $\alpha$-$Fe_2O_3$, and the peaks corresponding to Fe (0) became more apparent. Further, $Fe_3C$ became the prominent phase with an increased loading of $\alpha$-$Fe_2O_3$.

XRD patterns of the SI composites (Figure 1c) consist of peaks at 27.5, 36.1, 54.4, and 69.0°, which are assigned to the (110), (101), (211), and (301) planes of the rutile phase (JCPDS card No: 21-1276) in addition to the peaks corresponding to $Fe_3C$, Fe, and $Fe_3O_4$. The interlayer distance and the crystallite size calculated for the rutile phase are 0.3235 nm and 52.1 nm, respectively. The intensity of the peaks corresponding to graphitic carbon decreased, the peaks of $Fe_3O_4$ diminished, and generally, the intensity of the peaks belonging to the rutile phase increased when the loading of FTO also increased. The rutile phase of $TiO_2$, $Fe_3C$, and Fe became prominent with the increasing loading of FTO. When amorphous FTO was annealed at 800 °C in a normal atmosphere, a heterostructure of $Fe_2TiO_5/TiO_2$ was formed. However, when the same was mixed with sucrose and annealed at 800 °C in a flow of $N_2$, iron mainly reacted with carbon to form $Fe_3C$ and was reduced in the presence of carbon and $N_2$, while $TiO_2$ was separated. XRD patterns of the SFI composites are shown in Figure 1d. The patterns consisted of peaks corresponding to graphitic carbon, rutile, $Fe_3O_4$, $Fe_3C$, and Fe, of which the rutile phase of $TiO_2$ appeared to comprise broad peaks with low intensity compared to the XRD patterns of SI composites. This was due to the low loading of amorphous FTO and the good dispersion of the rutile nanoparticles. Other features were quite like those observed in XRD patterns of SI composites.

**4.2. TEM Analysis.** TEM images were collected to study morphology at the nanoscale. Figure 2a–c shows the arrangement of the graphitic carbon of SF 10, SI 10, and SFI 20. It could be seen that graphitic carbon arranged as nanoribbons with a width of about 10 nm is structured in a random orientation. These nanoribbons are bent and oriented in a circular-/oval-type shape, indicating they existed around nanoparticles. Very few nanoparticles were observed in the TEM images shown in the figure. However, graphitic carbon nanoribbons are distributed throughout the image. This observation suggests that the nanoparticles, which are the catalysts of graphitization crystallized amorphous carbon, migrate to another place and catalyze the graphitization of amorphous carbon. This phenomenon is called dissolution and precipitation, where amorphous carbon dissolves and reprecipitates as graphitic carbon. Therefore, abundant graphitic carbon nanoribbons are present with few nanoparticles. The high-resolution TEM (HRTEM) image of SI 10 is shown in Figure 2d.

The atomic planes are arranged with an interlayer distance of 0.34 nm, which is consistent with the d-spacing values reported in the XRD analysis. Indicated here is the presence of turbostratic carbon and not graphite since the d-spacing of graphite is 0.335 nm. Although turbostratic carbon has the ABABAB... hexagonal arrangement, one layer could be rotated or translated to another due to the orientation of the carbon layers in graphite being rigid.

Figure 2e illustrates the encapsulation of the nanoparticles by the graphitic carbon nanoribbons, while Figure 2f exhibits the HRTEM image of the graphitic carbon with distinguishable atomic planes. Figure 2g reveals the arrangement of graphitic carbon with respect to $Fe_3C$ nanoparticles, while Figure 2h shows the same with respect to $Fe_3O_4$. Meanwhile, Figure 2i highlights the proximity of the nanoparticles to graphitic carbon, and interestingly, it could be seen that small amounts of $Fe_2TiO_5$ with a d-spacing of 0.47 nm corresponding to the (200) plane are present though they were absent in the XRD patterns. Further, the junction of $Fe_2TiO_5$ and $Fe_3O_4$ was identified. $Fe_3C$ nanoparticles with a d-spacing of 0.20 nm with respect to the oriented graphitic carbon are shown in Figure 2j. Consequently, it is evident that the heterostructures are properly linked at the junctions and the graphitic carbon is orientated with respect to that. Figure 2k–m shows the selected area diffraction patterns of SF 2.5, SI 10, and SFI 20, respectively. They appear to have diffused rings, confirming the presence of a dispersed graphitic



https://doi.org/10.1021/acsomega.2c02336
ACS Omega 2022, 7, 25403−25421

carbon structure, while the dark spots indicate the polycrystallinity of metal oxides.

**4.3. SEM Analysis.** SEM images (Figure 3) were collected to study the morphology of the synthesized composites at a macroscale. SEM images of SF 10 at low and high magnifications are shown in Figure 3a,b, respectively. Iron prominent nanomaterials ($Fe_3C$, Fe, and $Fe_3O_4$) are distributed heterogeneously on the carbon matrix, where they are quite agglomerated. Upon increasing the incorporated loading of $Fe_2O_3$ in SF 1, the nanomaterials stated above produced as nanoplates appeared to be arranged as nanoplate macroballs (Figure 3c). At a higher magnification (Figure 3d), it could be observed that they are arranged in an orderly manner. As shown in the low- and high-magnification SEM images of SI 10, Figure 3e,f, respectively, irregular-shaped small nanoparticles are aggregated on the carbon support at a low loading of FTO. At a higher loading of FTO in SI 1, the carbon matrix is crowded by the aggregated irregular-shaped nanoparticles (Figure 3g,h). SFI composites are fabricated by adding both $Fe_2O_3$ and FTO to the sucrose solution.

At a lower loading in SFI 20, nanoparticles deposited on the carbon matrix are shown in Figure 3i,j. However, with a higher loading of both $Fe_2O_3$ and FTO, the presence of nanoplates of iron prominent nanomaterials ($Fe_3C$, Fe, and $Fe_3O_4$) was observed, but they have not been arranged as nanoplate microballs, which was evident with SF 1 (Figure 3k,l). The fabrication of the nanoplate microballs was interrupted by the presence of irregular-shaped nanoparticles produced by the addition of FTO. EDX spectra of SF 10 and SF 1 shown in Figure 3m,n illustrate only the presence of C and iron in the composites, having a higher iron content in SF 1 as expected. SI composites are prepared with the addition of FTO and at a lower loading of FTO in SI 10. This was in addition to C, Fe, and Ti being observed in the EDX spectrum (Figure 3o). However, with a higher loading of FTO, other elements such as Si, Mn, and Al were detected (Figure 3p). This is consistent with the XRF data tabulated in Table 1 and explained by the ilmenite in the raw material of FTO containing Si, Mn, and Al. A similar behavior was observed with SFI 20 and SFI 2, as shown in the EDX spectra (Figure 3q,r, respectively).

**Table 1. Metallic Composition of the Synthesized Materials as Metallic Oxides**

| material | % mass $Fe_2O_3$ | % mass $TiO_2$ | % mass MnO | % mass $V_2O_5$ | % mass $ZrO_2$ |
|---|---|---|---|---|---|
| FTO | 51.83 | 46.24 | 0.87 | 0.68 | 0.37 |
| SF 1 | 99.9 | | | | |
| SI 1 | 51.41 | 46.70 | 0.88 | 0.71 | 0.29 |
| SFI 2 | 81.47 | 16.68 | 0.84 | 0.69 | 0.32 |

**4.4. Resonant Raman Spectroscopy.** Resonant Raman spectroscopy is the major characterization technique used for different carbon materials including graphite,[42] graphene,[43] carbon nanotubes,[44] and amorphous carbon.[45] The Raman spectrum of SF 10 is shown in Figure 4a. Graphite and graphene-like carbon materials are composed of layers of $sp^2$ hybridized hexagons, and these layers are held together via van der Waals interactions. The main feature of the Raman spectrum of the carbon material is the appearance of D and G bands, which are centered at 1350 and 1580 $cm^{-1}$, respectively. The G band is a first-order Raman process due to the doubly degenerate longitudinal optical (LO) phonon mode occurring at the high-symmetry Γ point.[15,46] Further, the G band corresponds to the bond stretching of all pairs of $sp^2$ atoms in both rings and chains.[47] The D band is a second-order Raman process around the high-symmetry K-point involving defects and phonons of $A_{1g}$ symmetry. Moreover, the D band is attributed to the breathing modes of $sp^2$ atoms in hexagons.[46−48] The band that appears between the D and G bands is due to both $sp^2$ and $sp^3$ carbons that are not crystallized. It also occurs because of the hydrogen and oxygen in carbon.[46,49,50]

The pain parameter calculated to determine the crystallinity of carbon is the intensity ratio of the D and G bands ($I_D/I_G$), where the intensity represents the molecular vibrations entailed in the Raman process. Defects in two-dimensional (2D) lattices are categorized into two: zero-dimensional (0D) and one-dimensional (1D) defect. Point defects or 0D defects normally occur when graphene prepared by mechanical exfoliation of highly oriented pyrolytic graphite is exposed to ion bombardment at various doses. The distance between the nearest defects ($L_D$) or the defect density is used to characterize the point defects. In pristine graphene, $L_D$ is equal to infinity, while it is equal to zero in highly disordered graphene.[51] Turbostratic carbon prepared by heat treatment of amorphous carbon is rich with ID defects, and they are characterized by their average crystallite size ($L_a$) and crystallite area ($L_a^2$). $L_a$, being like $L_D$, is equal to infinity in pristine graphene and equal to zero in highly disordered graphene. $L_D$ and $L_a$ are calculated according to equation numbers 1 and 2, respectively.[51−53]

The main characteristic feature that governs the categorization of carbon from amorphous carbon to graphite is the $sp^2$-to-$sp^3$ ratio. Highly amorphous carbon with the highest $sp^3$ content (80−90%) is called the tetrahedral amorphous carbon (ta-c), and it is considered that the $sp^3$ content in graphite is zero. When the amorphization trajectory is taken into account, it has three main transformations: (i) graphite to nanocrystalline graphite (nc-G); (ii) nc-G to amorphous carbon (a-C); and (iii) a-C to ta-C. Graphite and nc-G consist of 0% $sp^3$, while a-C contains about 20% $sp^3$ carbon.[46] $I_D/I_G$ diminishes when an amorphous carbon material becomes better organized and converts to a more crystalline carbon. There is further improvement in the crystallinity where the nanocrystalline carbon material transforms to graphitic carbon, and the ratio again diminishes.[46] The observation of decreasing $I_D/I_G$ with an increased loading of catalyst (of graphitization) is apparent in all three types of carbon materials synthesized, SF, SI, and SFI, as shown in Figure 4b−d, respectively. $I_D/I_G$ decreases with increasing iron loading when the amorphous carbon materials become more organized and form nc-G as in S to SF 2.5, S to SI 1.25, and S to SFI 2.5. The graphitic nature of nc-G becomes increasingly like graphite, while a further rise in the loading of iron and $I_D/I_G$ wanes. This is indicated in the above figures (SF 1 to SF 1.25, SI 1 to SI 1.25, and SFI 2 to SFI 2.5).

The $L_a$ of all three types of composites also increased with an increased loading of the catalyst, as shown in Figure 4e−g. A similar behavior was observed with $L_D$ as well (Figure 4h−j). Behaviors of both $L_a$ and $L_D$ further support the observation made with the variation of the $I_D/I_G$ ratio. Moreover, Figure 4k−m indicates the variation of the density of the 0D defects ($1/L_D^2$) as a function of the crystallite area ($L_a^2$) of SF, SI, and SFI composites, respectively. The density of the 0D defects decreases with increasing crystallite area, i.e., with increasing iron loading, thus supporting the behavior suggested by the variation of $I_D/I_G$. In this way, the area of crystallinity expands with an increasing catalyst loading. With a reduction in 0D


https://doi.org/10.1021/acsomega.2c02336
ACS Omega 2022, 7, 25403−25421

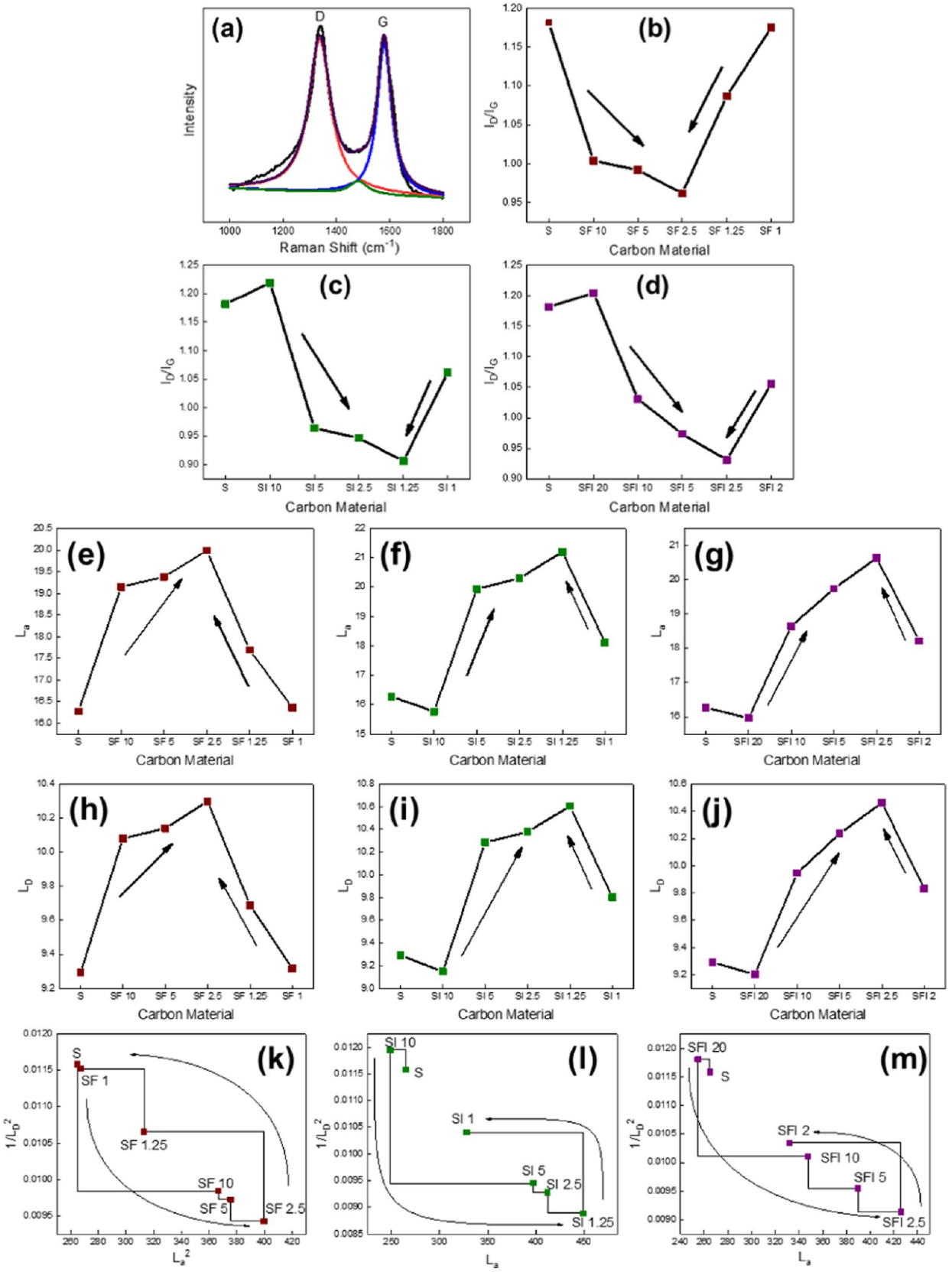


**Figure 4.** (a) Peak deconvolution of SF 10. Variation of $I_D/I_G$ of (b) SF, (c) SI, and (d) SFI composites. Variation of $L_a$ of (e) SF, (f) SI, and (g) SFI composites. Variation of $L_D$ of (h) SF, (i) SI, and (j) SFI composites. $1/L_D^2$ vs $L_a^2$ of (k) SF, (l) SI, and (m) SFI.

defects, the material is dominated by 1D defects. Explaining the above-mentioned observations, it is evident that SF materials become more organized and convert to nc-G when the sucrose-to-$Fe_2O_3$ ratio increases to 1.25:1. With a further decrease in the ratio (1:1), the percentage of nc-G increased, and the crystallinity moved toward graphite, which increased the degree



https://doi.org/10.1021/acsomega.2c02336
ACS Omega 2022, 7, 25403−25421

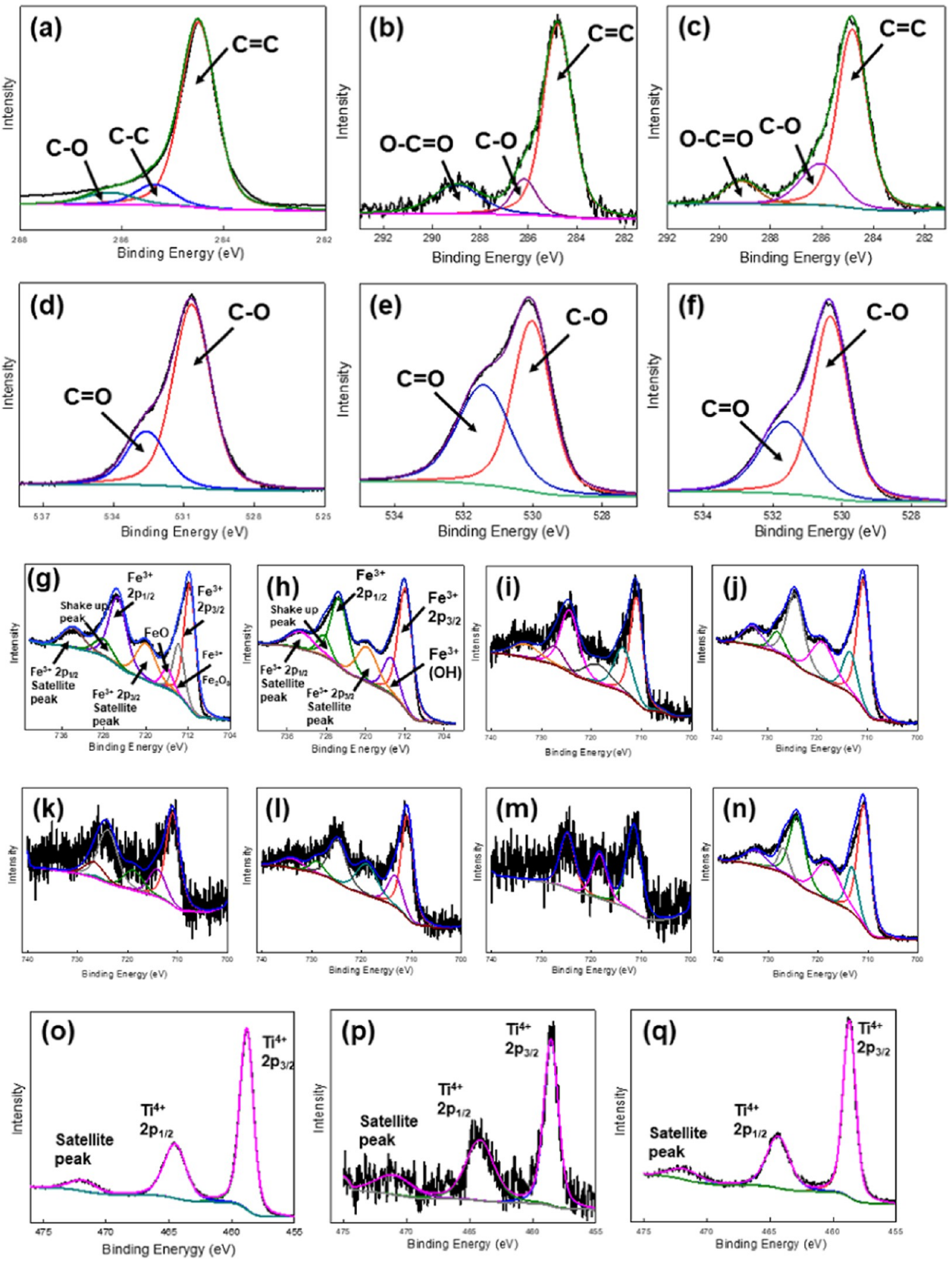


**Figure 5.** continued



https://doi.org/10.1021/acsomega.2c02336
*ACS Omega* 2022, 7, 25403−25421

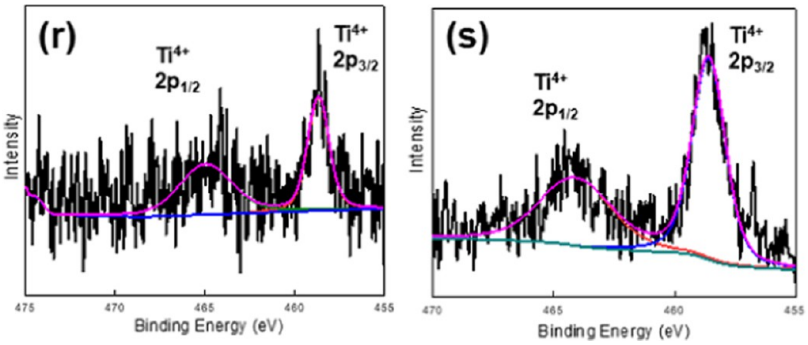


**Figure 5.** High-resolution spectra of C 1s of (a) amorphous carbon (S), (b) $\alpha$-$Fe_2O_3$, and (c) FTO. High-resolution spectra of O 1s of (d) amorphous carbon, (e) $\alpha$-$Fe_2O_3$, and (f) FTO. High-resolution spectra of Fe 2p of (g) FTO, (h) $\alpha$-$Fe_2O_3$, (i) SF 10, (j) SF 1, (k) SI 10, (l) SI 1, (m) SFI 20, and (n) SFI 2. High-resolution spectra of Ti 2p of (o) FTO, (p) SI 10, (q) SI 1, (r) SFI 20, and (s) SFI 2.

of graphitization. A similar behavior was observed with SI and SFI. However, the nc-G state appeared in SI materials when the sucrose-to-ilmenite ratio is 1:1 and in SFI when sucrose to $Fe_2O_3$, and the ilmenite product ratio is 2:1:1 (sucrose to metal oxide ratio 2:1).

Two methods describe catalytic graphitization, and these are the dissolution−precipitation mechanism and the carbide formation−decomposition mechanism. Fe from $Fe_2O_3$ and the ilmenite product, and Ti from the ilmenite product, catalyzes the graphitization in two different ways. Fe, which belongs to Group VIII, contains six electrons in the d orbitals, and the electron configuration would scarcely change by accepting electrons from carbon and instead of carbon dissolving as positive ions. Therefore, Fe catalyzes graphitization via the dissolution−precipitation mechanism. However, Ti, which belongs to Group IV, contains two electrons in the d orbital and forms strong chemical bonds with carbon, resulting in metal carbide, TiC.[14] Based on this, it can be stated that the ratio between the carbon source, sucrose, to the catalyst, which is required to catalytically graphitize amorphous carbon to produce nc-G, is 1:1.

$$\frac{I_D}{I_G} = (102 \mp 2)/L_D^2 \quad (1)$$

$$L_a(\text{nm}) = (2.14\times10^{-10}) \times \lambda_{\text{laser}}^4 \times \left(\frac{I_D}{I_G}\right)^{-1} \quad (2)$$

**4.5. XPS Analysis.** The surface of the synthesized composites was analyzed by XPS to study the chemical environment of the elements of interest. The higher-resolution spectrum of C 1s of the amorphous carbon (Figure 5a) was deconvoluted into three peaks centered at 284.5, 285.4, and 286.2 eV, which are attributed to C−C/C═C, C−H, and C−O, respectively.[55] It was well noted that the positions of the peaks after deconvolution of carbon 1s in pure carbon and containing composites differed from that of pure $\alpha$-$Fe_2O_3$ and FTO (Figure 5b,c, respectively), where the three peaks appeared at 284.8, 286.1, and 289.14 eV and 284.8, 286.2, and 288.9 eV, respectively. These binding energies represent the C−C/C═C, C−O, and COOH/COOR, respectively. The peak corresponding to the C−H is missing in $\alpha$-$Fe_2O_3$ and FTO. Consequently, it is evident that the C−H chemical environment is present in carbon materials only. The peaks at 530.65 and 532.59 eV in the higher-resolution spectrum of O 1s of amorphous carbon (Figure 5d) are assigned to the oxygen bound to C. The convolution of O 1s of $\alpha$-$Fe_2O_3$ and FTO (Figure 5e,f, respectively) was similar to that of Figure 5d.

The higher-resolution spectrum of Fe 2p of FTO is shown in Figure 5g, which is deconvoluted to several peaks. Peaks at 711.7 and 725.5 eV represent the spin−orbital coupling of the P orbital as $2p_{3/2}$ and $2p_{1/2}$ of $Fe^{3+}$, while the peaks at 720.2 and 734.1 eV are assigned to the satellite peaks of them, respectively. The peak at 713.9 eV is reported to be present in $\alpha$-$Fe_2O_3$, while the peak at 716 eV could be attributed to FeO.[56] The peak at 728.45 eV could be considered a shake-up peak. The peak deconvolution of Fe 2p of $\alpha$-$Fe_2O_3$ (Figure 5h) is quite similar to that of FTO except for the peaks at 713.9 and 716 eV being absent and the peak at 715 eV, which corresponded to the $Fe^{3+}$ and associated with $OH^-$, being present.[56] Peak deconvolutions of the higher-resolution spectrum of $Fe^{3+}$ of SF 10, SF 1, SI 10, SI 1, SFI 20, and SFI 2 are given in Figure 5i−n, respectively, and represent the presence of $Fe^{3+}$ on the composites' surface. The presence of $Ti^{4+}$ on the surface of FTO is confirmed by the higher-resolution spectrum of Ti 2p (Figure 5o). Peaks at 458.8 and 464.5 eV show the spin−orbital coupling of $Ti^{4+}$, $2p_{3/2}$ and $2p_{1/2}$, respectively.[57] The satellite peak appeared at 471.8 eV. Peak deconvolutions of the higher-resolution spectrum of $Ti^{4+}$ of SI 10, SI 1, SFI 20, and SFI 2 are exhibited in Figure 5p−s, respectively, and confirm the presence of $Ti^{4+}$.

**4.6. XRF Analysis.** XRF analysis was done to analyze the metallic contents in the synthesized materials. Collected data are summarized in Table 1. The main metallic compounds present in the precipitate obtained after ilmenite was treated with HCl followed by the addition of $NH_3$ (FTO) contain mainly Fe and Ti. Also, Mn, V, and Zr are present as impurities in ilmenite sand. The quantitative distribution of the above elements originated by adding product (I), which is the same in SI 1 and SFI 2. However, the mass percentage of Fe is approximately 30% greater than that in both I and SI 1, while the mass percentage of Ti is smaller in the same amount due to the addition of $Fe_2O_3$ externally. SF 1 contains only Fe since the metallic compound is consistent with the synthesis procedure.

**4.7. DRS Analysis.** Diffuse reflectance spectra of the synthesized samples were acquired to study the absorption behavior of the synthesized materials. Supporting Information Figure S1a−d shows the UV−visible absorption spectra of the synthesized materials. The absorption spectrum of pure $TiO_2$ prepared by the sol−gel method annealed at 800 °C serves as the reference. It shows significant UV absorption with an absorption edge of 415 nm. Observed here is that the synthesized materials exhibit optical absorption in the visible range. Tauc plots ($(F(R) \times h\nu)n$ vs $h\nu$) were constructed for both direct and indirect transitions to determine the band gaps of the synthesized materials. $n$ = 2 was used to plot the graphs for the direct


https://doi.org/10.1021/acsomega.2c02336
ACS Omega 2022, 7, 25403−25421

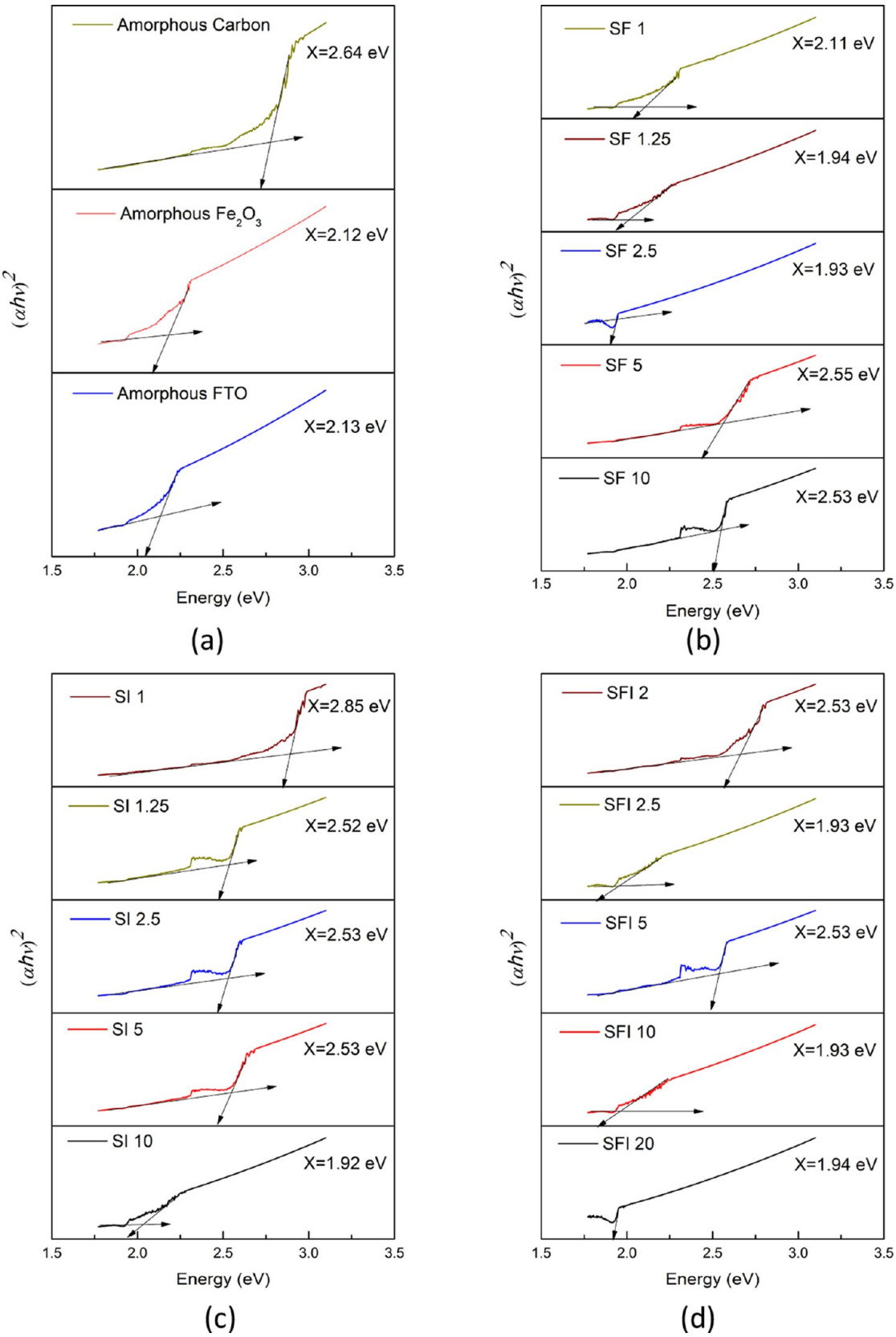


**Figure 6.** Direct transitions of (a) amorphous materials (b) SF, (c) SI, and (d) SFI composites.

transitions (Figure 6), and $n = 1/2$ was used to construct the plots representing the indirect transitions (Supporting Information Figure S1e–h). Band gaps were calculated according to the method proposed by Makula et al.[58] The behaviors of the graphs demonstrate that the synthesized materials show direct transitions. Pure $TiO_2$ exhibits a band gap of 2.98 eV, which is consistent with the value reported for the rutile,[59] and the band



https://doi.org/10.1021/acsomega.2c02336
ACS Omega 2022, 7, 25403−25421

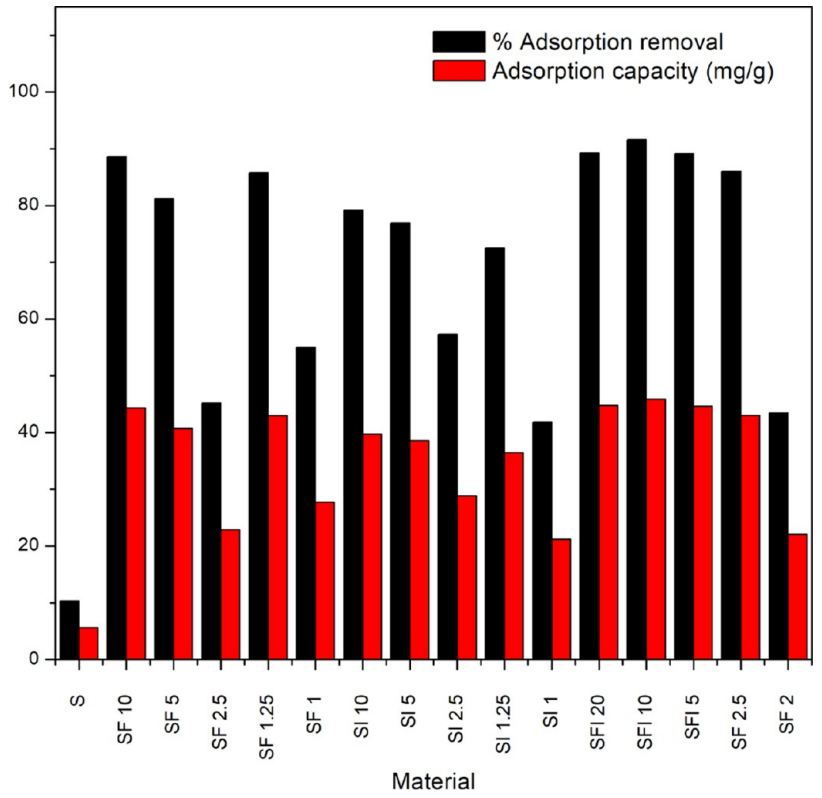


**Figure 7.** Percentage adsorption removal and adsorption capacity of the synthesized composites.

gaps for FTO and $\alpha$-$Fe_2O_3$ were found to be 2.13 and 2.12 eV, respectively.

The band-gap value obtained for the highly amorphous carbon (SC) is 2.64 eV. The synthesized carbon-based composites, i.e., SF, SI, and SFI, showed, first, that the band-gap values are in the range of 1.92−2.85 eV and, second, a clear trend in the band-gap values with respect to the metal content was not observed.

The main metallic crystalline compounds present in the SF, SI, and SFI composites and the crystallized carbon contribute to the overall band-gap value resulting for each material. The amount of such materials present in the sample would vary from place to place because the synthesized materials are heterogeneous, as revealed by TEM analysis. Further, the overall dispersity of each chemical formula affects the band-gap values. The size of the nanoparticles greatly affects the band gap, where the band-gap values increase as the particle size decreases. Holes in the valence band and electrons in the conduction band become confined with decreasing particle size, and due to this confinement in the electrons and holes, the band gap between the valence and conduction bands increases. The shape of the nanomaterials contributes to the band-gap values.

The volume-to-surface-area ratio varies as the size and shape of the nanomaterials change, which contributes to the variation in the number of surface atoms and hence the cohesive energy. Therefore, the band gap varies at the nanoscale due to the change in the size and shape.[60] Further, the graphitic carbon present contributes to the band gap, and the amount of graphitic carbon present varies from sample to sample and from location to location in the same sample, leading to variation in the band-gap value. It could be considered that when the percentage of the metallic compounds increases the band-gap value is mainly governed by the metallic compounds since the collected sample for the DRS analysis may contain more of the metallic compounds with less carbon due to the heterogeneous distribution.

With this in mind, it is evident that many factors affect the band-gap values of the synthesized materials. Band-gap values of SF composites decreased up to SF 1.25 and then increased at SF 1. The band-gap value of SI composites keeps increasing with increasing metal content. Band-gap values of SFI composites have no trend and fluctuate with increasing metal content. The main metallic components of the SF complex are $Fe_3C$, Fe, and $Fe_3O_4$. SI and SFI composites consist of $TiO_2$ in addition to the above metallic components, which also significantly contribute to the band-gap values. The sample used to measure absorbance may contain more carbon or more metallic species due to two things: first, the heterogeneous distribution; and second, the variation in the percentage of the metallic species with respect to the carbon content. The end result is no clear trend in the band-gap values. Further, as mentioned above, the band gap is a net result of many factors and hence a clear trend was not observed in any of the composites synthesized.

**4.8. Photocatalysis.** Synthesized amorphous carbon and the composites were shaken in 50 mL of 100 ppm MB solution for 16 h. Figure 7 shows the percentage MB removed and the catalysts' adsorption capacities. Amorphous carbon prepared by pyrolyzing only sucrose showed the least adsorption of MB (10.3%). Composites SF, SI, and SFI showed larger removals of MB ranging from 41 to 91%. The adsorption capacities ($q_e$) of all of the adsorbents are summarized in Table 2. The smallest adsorption capacity was obtained for amorphous carbon (5.57 mg/g) and that of the composites varied in the 21.18−45.87 mg/g range. Obtained adsorption capacities are much higher than some of the reported values of the same type of materials as tabulated in Table 2.



https://doi.org/10.1021/acsomega.2c02336
ACS Omega 2022, 7, 25403−25421

**Table 2. Comparison of the Obtained Adsorption Capacities with the Same Reported in the Literature**

| adsorbent | adsorption capacity (mg/g) | reference |
|---|---|---|
| SI 1 | 21.18 | this work |
| SFI 10 | 45.87 | this work |
| turbostratic carbon/$Fe_3C$/Fe | 17.8 | 12 |
| iron impregnated AC | 176.37 | 61 |
| hydrogen-titanate nanofibers | 17.8 | 62 |
| graphitic carbon encapsulated $Fe_3C$ | 33.1 | 63 |
| $TiO_2$/carbon | 15.24 | 64 |
| $TiO_2$/graphene-like bamboo charcoal | 33.26 | 65 |

As reported in our previous study, MB adsorption to graphitic carbon/$Fe_2O_3$ follows a pseudo-second-order kinetics, where MB molecules adsorb via physisorption and /or chemisorption,[66−68] while that of amorphous carbon obeyed the pseudo-first-order kinetics model. During graphitization, the carbon material becomes better organized and forms graphene-like planes, as shown in the TEM images (Figure 2d). Hence, the planar MB molecules form $\pi-\pi$ interactions facilitating the chemisorption. As revealed by the Raman analysis, the degree of graphitization increased as the loading of the catalysts ($Fe_2O_3$ and FTO) increased. Subsequently, a new porous structure would be established including more micropores and mesopores in the composites. However, as tabulated in Table 2, the percentage of adsorption of MB does not increase with a larger loading of the catalyst, which is despite the amount of graphitic carbon formed increasing when the catalyst loading also increases.

Adsorption of MB is greater than 40% in all three types of composites, i.e., SF, SI, and SFI. In addition to the $\pi-\pi$ interactions, electrostatic interactions and van der Waals forces can also be formed in between the carboxyl and hydroxyl functional groups and MB molecules. The adsorption of MB to the prepared adsorbents is illustrated in Scheme 1. Generally,

**Scheme 1. Adsorption Mechanism of MB to Graphitic Carbon**

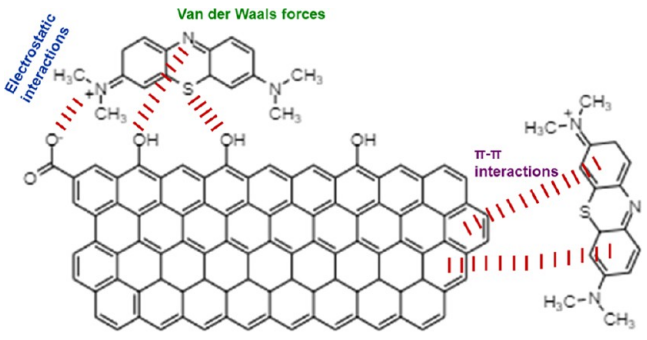


MB adsorption is high in composites with low catalyst loadings, and this is due to the presence of graphitic carbon and high porosity. In composites with a higher loading of the catalysts, graphitic carbon and porous structures get masked with the nanoparticles present, which reduces the effective surface area and active sites. The outcome is less adsorption of MB. SF composites consist of Fe, $Fe_3C$, and $Fe_3O_4$ nanoparticles distributed on a graphitic carbon matrix. SI and SFI composites contain $TiO_2$ in addition to the Fe, $Fe_3C$, and $Fe_3O_4$ nanoparticles. All photocatalysts are sensitive to sunlight since they comprise both UV and visible light. Photogenerated electrons and holes are produced upon exposure to sunlight. Electrons react with the oxygen adsorbed to the catalyst surface and atmospheric oxygen to produce intermediate superoxide radicals ($O_2^{\bullet-}$). Hydroperoxyl radicals ($HO_2^{\bullet}$) are formed when $O_2^{\bullet-}$ radicals react with $H^+$ produced from the dissociation of water. Hydroperoxyl radicals produce $H_2O_2$.

Holes react with water adsorbed and produce hydroxyl radicals ($OH^{\bullet}$). These radicals react with the MB molecules and degrade them to $CO_2$, $SO_4^{2-}$, $NH_4^+$, and $NO_3^-$ under sunlight.[69] Graphitic carbon plays a crucial role in photocatalysis. The reactant MB molecules should be near the reactive radicals. As graphitic carbon enhances the adsorption of MB, radicals can easily degrade MB into products. Moreover, since graphitic carbon is conductive, the electrons generated at the photocatalysts are readily absorbed by the graphitic carbon. This enhances the charge separation, and such electrons migrate on the graphitic carbon matrix because of the high conductivity, thus increasing the photocatalytic activity. Graphitic carbon itself is conductive, and the layers are located at a 0.34 nm distance from each other. Consequently, they can contribute to the production of photogenerated electrons and holes. Hence, the photocatalytic activity is increased when graphitic carbon is present. The first-order kinetic plots of SF, SI, and SFI composites are shown in Figure 8a−c, respectively. When SF composites are considered, SF 10 showed the lowest rate constant (0.004 $min^{-1}$) caused by the inadequate presence of graphitic carbon and the catalysts. This led to the production of small concentrations of electrons and holes.

The maximum activity resulted with SF 5 (0.007 $min^{-1}$), as its adsorption capacity is also high and contains the desired amount of photocatalysts distributed on the graphitic carbon matrix, thereby enhancing both the photogenerated electron and hole pair production. It also facilitated the separation of electrons and holes, minimizing the electron−hole pair recombination. The rate constants for the photodegradation of MB in the presence of the other three SF composites with high loading of the catalysts are comparatively lower, which is explained by the blockage of the graphitic carbon, porous structure, and electron−hole pair recombination. Further, high loading of the metal nanoparticles aggregated decreased the effective surface area, which generated less photocatalytic activity. The highest rate constants among the SI and SFI catalysts were observed in the presence of SI 10 (0.007 $min^{-1}$) and SFI 20 (0.005 $min^{-1}$), respectively. However, with SI and SFI composites, the photocatalytic activity increased at SI 1 and SFI 2 although a reduction was observed for SI 1.25 and SFI 2.5. This occurred because the number of electrons and holes generated each time is higher with those composites. The rate constants for photodegradation of MB in the presence of catalysts are tabulated in Table 3.

It cannot be assumed that the band gap significantly affects the photocatalytic activity of the composites because the nano-photocatalysts are dispersed and immobilized on the graphitic carbon matrix, instead of forming heterostructures in which all of the nanomaterials of different compositions and crystallographic orientations are merged. In all types of composites, initially, a low rate of reaction was observed, and over time, the photocatalytic rate increased. Initially, the active sites were saturated as the catalysts were shaken in 100 ppm of MB. Once the catalysts in 10 ppm of MB are exposed to sunlight, MB molecules (which already have been adsorbed) get degraded and cause a minimal reduction in the absorbance of the 10 ppm MB solution, of which the absorbance is measured during the


https://doi.org/10.1021/acsomega.2c02336
ACS Omega 2022, 7, 25403−25421

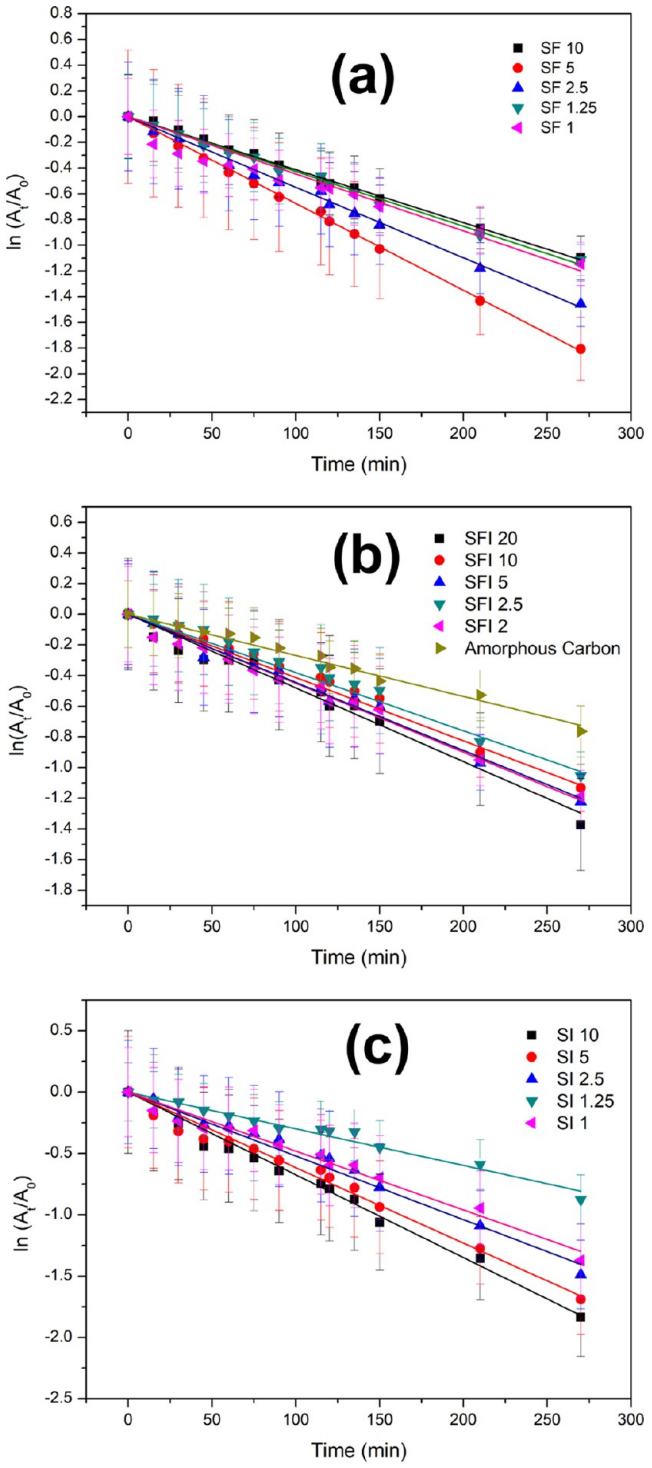


**Figure 8.** First-order kinetic plots of (a) SF, (b) SI, and (c) SFI composites.

reaction. Once the preadsorbed MB molecules degraded, the subsequently created vacant active sites would adsorb MB molecules in the solution and photodegrade them, resulting in a higher rate of reaction. The above observations suggest there is a clear relationship between the adsorption of the dye molecules to the graphitic carbon and photocatalysis. It is evident that rather than removing dyes from only adsorption or photocatalysis, fabricating a composite that could remove dyes from both adsorption and photocatalysis using natural substances is innovative and more applicable for decontaminating water from textile dyes.

**Table 3. Rate Constant for Photodegradation of MB in the Presence of Synthesized Materials**

| material | rate constant ($min^{-1}$) |
|---|---|
| SF 10 | 0.004 |
| SF 5 | 0.007 |
| SF 2.5 | 0.005 |
| SF 1.25 | 0.004 |
| SF 1 | 0.005 |
| SI 10 | 0.007 |
| SI 5 | 0.006 |
| SI 2.5 | 0.005 |
| SI 1.25 | 0.003 |
| SI 1 | 0.005 |
| SFI 20 | 0.005 |
| SFI 10 | 0.004 |
| SFI 5 | 0.004 |
| SF 2.5 | 0.003 |
| SF 2 | 0.004 |

**4.9. Mechanism of Photodegradation.** SF photocatalysts comprise Fe, $Fe_3C$, and $Fe_3O_4$, while SI and SFI catalysts contain $TiO_2$ in addition to Fe, $Fe_3C$, and $Fe_3O_4$. These nanoparticles are well distributed on the graphitic carbon matrix. Upon exposure to sunlight, $TiO_2$ nanoparticles excite electrons from VB to the CB, while Fe, $Fe_3C$, and $Fe_3O_4$ do the same utilizing the visible irradiation. $TiO_2$ located in the junction with Fe, $Fe_3C$, and $Fe_3O_4$ facilitates the charge separation, enhancing the photocatalytic activity. High conductivity of the graphitic carbon matrix facilitates the migration of electrons to the molecular oxygen and water to produce superoxide radicals ($O_2^{\bullet-}$) and hydroperoxyl radicals ($HO_2^{\bullet}$), respectively, while holes are passed to water adsorbed and to produce hydroxyl radicals ($OH^{\bullet}$). Further, as the MB molecules are adsorbed to the graphitic carbon support, they easily react with the produced radicals and get degraded to harmless products ($CO_2$, $SO_4^{2-}$, $NH_4^+$, and $NO_3^-$) as shown in Scheme 2.

**Scheme 2. Mechanism of Photodegradation of MB by the Photocatalysts under Sunlight**

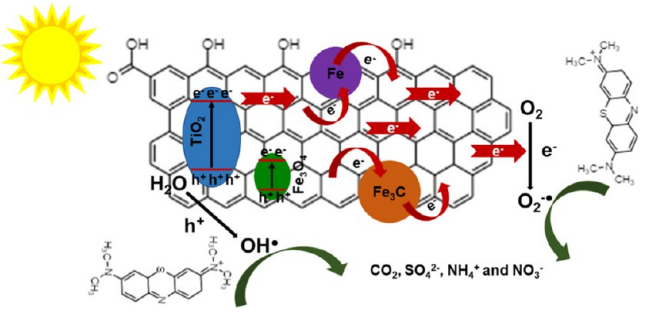


XPS data were evaluated to further support the proposed mechanism. The binding energy of Fe $2p_{3/2}$ of pure $Fe_3O_4$ is reported to be present at 710.2 eV.[56] An increase in the binding energy of Fe $2p_{3/2}$ in both SI 10 and SFI 20 by 0.75 and 1.28 eV, respectively, was observed, indicating a reduction in the electron concentration (Figure 5k,m, respectively).[70] The binding energy of Fe $2p_{3/2}$ of Fe(0) is reported to be at 706.6 eV.[56] The XPS feature of $Fe_3C$ appeared at 708.5 eV.[71] Despite these peaks not being present in the higher-resolution spectra of Fe $2p_{3/2}$ of both



https://doi.org/10.1021/acsomega.2c02336
ACS Omega 2022, 7, 25403−25421

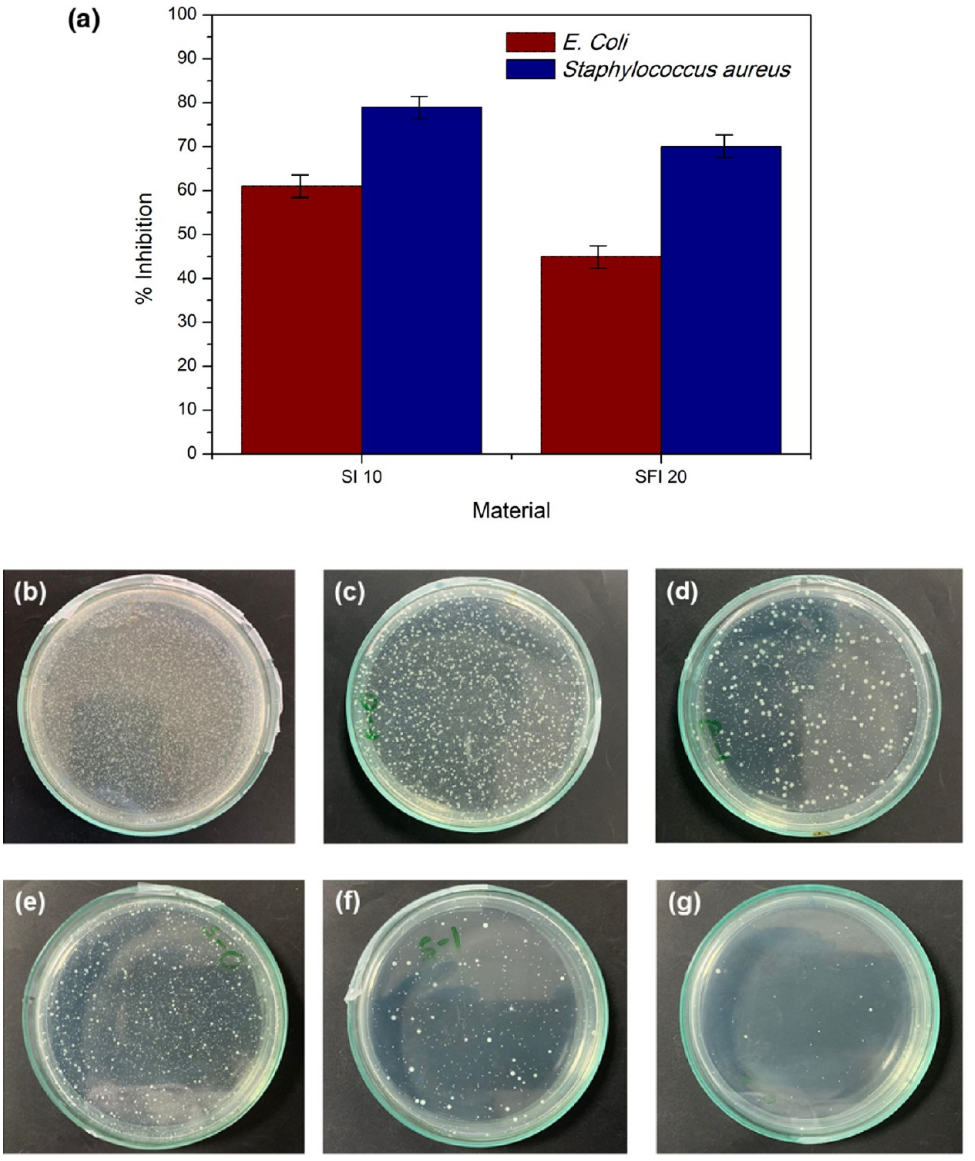


**Figure 9.** (a) Percentage inhibition of *E. coli* and *S. aureus* by SI 10 and SFI 20 composites-broth dilution method, sterilization performance of *E. coli*, (b) the blank experiment (c) SFI 20 (d) SI 10, sterilization performance of *S. aureus* (e) the blank experiment (f) SFI 20 (g) SI 10.

SI 10 and SFI 20 due to the low concentration, the binding energy of Fe $2p_{3/2}$ appeared at 710.95 and 711.48 eV, respectively. These were higher than the expected value and exhibited a low electron concentration. Therefore, given that the electron density at iron-based species is low, it suggests that photogenerated electrons at those sites are readily taken by the graphitic carbon, leading to the production of $O_2^{\bullet-}$, which degrades MB as proposed by the mechanism. The binding energy of Ti $2p_{3/2}$ of pure $TiO_2$ is reported to be present at 459.36 eV.[71] However, the peak positions of Ti $2p_{3/2}$ of both SI 10 and SFI 20 appeared at 458.55 and 458.7 eV, respectively (Figure 5p,r), revealing a downshift of the binding energy by 0.81 and 0.66 eV, respectively. It suggests that $TiO_2$ is enriched with electrons.[70] Hence, generation of the $O_2^{\bullet-}$ occurs at the CB band of $TiO_2$, while $OH^{\bullet}$ radicals are generated at the VB.

**4.10. Antibacterial Activity.** SI 10 and SFI 20 composites were selected to determine the antibacterial activity of the synthesized composites as they comprised $TiO_2$-$Fe_3C$-Fe-$Fe_3O_4$/graphitic carbon. They also showed the highest rates of photodegradation in each category. The antibacterial activity was tested on inhibition of Gram-negative *E. coli* and Gram-positive *S. aureus* bacteria under the illumination generated by a 100 W LED light. The antibacterial activity could be caused by four different mechanisms by nanomaterials: (1) the nanocomposites disrupting the cell wall; (2) migration of nanocomposites into the cells and interfering with the ribosomes, DNA replication, and interrupting ATP production; (3) reactive oxygen species disrupting the membrane; and (4) perforating of the membrane. The tested nanomaterials can inhibit the bacteria especially by mechanism 3 once exposed to light. The antibacterial activity of the selected composites is shown in Figure 9, and experiments were conducted in triplicates. SI 10 inhibited 61% of the *E. coli*, while only 42% was inhibited by SFI 20. The antibacterial activity of both SI 10 and SFI 20 was higher in discouraging the growth of *S. aureus* when compared to *E. coli*, with the percentages being 79 and 70%, respectively. Both composites can inhibit the growth of Gram-negative and Gram-positive bacteria. The broths resulting from the broth dilution method were cultured on nutrient agar plates to quantify the viable cells present after the inhibition caused by the


https://doi.org/10.1021/acsomega.2c02336
ACS Omega 2022, 7, 25403−25421

nanocomposites. All of the bacteria in the blank experiments of both *E. coli* and *S. aureus* were live after illumination, as shown in Figure 9b,e, respectively, indicating that there is no or minimal impact of visible light on destroying both bacterial species. The images of plates with colonies shown in Figure 9c,d correspond to the inhibition of *E. coli* caused by both SI 10 and SFI 20, respectively. They indicate a decrease in the number of colonies of *E. coli*, representing 69 and 50% inhibition, respectively. Similarly, as shown in Figure 9f,g, respectively, there is a significant reduction of colonies of *S. aureus* demonstrating 92 and 84% inhibition, respectively, for SI 10 and SFI 20. The obtained percentages of inhibition by the colony count are higher than those resulting from the broth dilution method because the optical density measured at the broth dilution method is a measure of both living and nonliving cells, while the colony count method represents only the viable cells. Therefore, it is evident that the nanocomposites have inhibited both *E. coli* and *S. aureus*. Further, to visualize the inhibition action caused by the composites (SI 10) on *E. coli*, SEM images were taken (Supporting Information Figure 2a,b). Areas where the nanocomposites colloid with the bacterial cell and cause physical damage are highlighted in red-color circles. Although SI 10 and SFI 20 have the same composition, the antibacterial activity of SI 10 is greater than that of SFI 20. The difference in the synthesis is that SI composites were fabricated by mixing sucrose with amorphous FTO, while additionally, amorphous $Fe_2O_3$ was added in the synthesis of SFI composites. The rate of photocatalysis of SI 10 (0.0068 $min^{-1}$) is greater than that of SFI 20 (0.0048 $min^{-1}$). Radicals are mainly responsible for the photodegradation of MB, and more radicals are formed in the presence of the SI 10 catalyst than that of SFI 20, as revealed by the results of photocatalysis. Based on this, it could be concluded that the mechanism, disruption of the membranes by the reactive oxygen species, is higher in SI 10 than in SFI 20, resulting in higher antibacterial activity in the former than in the latter. Thus, fabricated composites can not only remove dyes from wastewater but also inhibit the growth of harmful bacteria from wastewater as well.

## 5. CONCLUSIONS

In conclusion, we have demonstrated the fabrication of $TiO_2$-$Fe_3C$-Fe-$Fe_3O_4$/graphitic carbon composites using natural ilmenite sand and sucrose as the raw materials, varying the weight ratio between sucrose and the product obtained by treating the acid leach of ilmenite with ammonia. Along with that, $Fe_3C$-Fe-$Fe_3O_4$/graphitic carbon composites were also successfully synthesized by mixing sucrose with $Fe_2O_3$. Further, both $Fe_2O_3$ and the product obtained by treating the acid leach of ilmenite with ammonia were also mixed with sucrose, varying the weight ratios. All of the composites were effective in removing MB via adsorption and photocatalysis. SFI 10 indicated the highest adsorption capacity of 45.87 mg/g removing 91.6% of MB, while SF 10 exhibited 44.33 mg/g adsorption capacity removing 88.6% of MB, the highest in the SF category. $\pi-\pi$ interactions between the graphitic carbon and MB enhanced the chemisorption.

The highest adsorption capacity of the SI group was obtained with SI 10 (39.72 mg/g), which removed 79.2% of MB. The synthesized composites were effective in degrading MB under photocatalysis. The highest rate constant for photodegradation of MB was achieved with SF 5 and SI 10 (0.0068 $min^{-1}$), while SFI 20 showed the highest rate constant (0.0048 $min^{-1}$) in its category. Electrons photogenerated by $TiO_2$, Fe, $Fe_3C$, and $Fe_3O_4$ migrate on the conductive graphitic carbon matrix generating $O_2^{\bullet-}$ and $HO_2^{\bullet}$ radicals. Holes further generate $OH^{\bullet}$ by reacting with the water adsorbed. These radicals photodegraded MB molecules effectively under sunlight. The synthesized composites were effective in inhibiting the growth of *E. coli* and *S. aureus*. Hence, fabricated composites using ilmenite and sucrose constitute an environmentally friendly and cost-effective strategy for removing dyes from wastewater and inhibiting the growth of bacteria.

## ASSOCIATED CONTENT

### Supporting Information

The Supporting Information is available free of charge at https://pubs.acs.org/doi/10.1021/acsomega.2c02336.

Diffuse reflectance absorption spectra, Tauc plots indicating the indirect transitions of the synthesized composites, and scanning electron microscopic images showing the antibacterial activity of nanocomposites (PDF)

## AUTHOR INFORMATION


### Corresponding Author

**Charitha Thambiliyagodage** − *Faculty of Humanities and Sciences, Sri Lanka Institute of Information Technology, Malabe 10115, Sri Lanka;* orcid.org/0000-0003-0906-4441; Email: charitha.t@sliit.lk

### Authors

**Leshan Usgodaarachchi** − *Department of Materials Engineering, Faculty of Engineering, Sri Lanka Institute of Information Technology, Malabe 10115, Sri Lanka*

**Madara Jayanetti** − *Faculty of Humanities and Sciences, Sri Lanka Institute of Information Technology, Malabe 10115, Sri Lanka*

**Chamika Liyanaarachchi** − *Faculty of Humanities and Sciences, Sri Lanka Institute of Information Technology, Malabe 10115, Sri Lanka*

**Murthi Kandanapitiye** − *Department of Nano Science Technology, Wayamba University of Sri Lanka, Kuliyapitiya 60200, Sri Lanka*

**Saravanamuthu Vigneswaran** − *Faculty of Engineering, University of Technology Sydney (UTS), Broadway, NSW 2127, Australia; Faculty of Sciences & Technology (RealTek), Norwegian University of Life Sciences, Ås 1430, Norway*

Complete contact information is available at: https://pubs.acs.org/10.1021/acsomega.2c02336



### Funding

This research was supported by the Accelerating Higher Education Expansion and Development (AHEAD) Operation of the Ministry of Higher Education funded by the World Bank.

### Notes

The authors declare no competing financial interest.

## ACKNOWLEDGMENTS

The authors acknowledge the Sri Lanka Institute of Nanotechnology, University of Peradeniya, and Wayamba University of Sri Lanka for providing the instrument facilities.


## REFERENCES

(1) Liang, C.; Chen, Y.; Wu, M.; Wang, K.; Zhang, W.; Gan, Y.; Huang, H.; Chen, J.; Xia, Y.; Zhang, J.; Zheng, S.; Pan, H. Green

Synthesis of Graphite from $CO_2$ without Graphitization Process of Amorphous Carbon. *Nat. Commun.* **2021**, *12*, No. 119.
(2) Long, W.; Fang, B.; Ignaszak, A.; Wu, Z.; Wang, Y. J.; Wilkinson, D. Biomass-Derived Nanostructured Carbons and Their Composites as Anode Materials for Lithium Ion Batteries. *Chem. Soc. Rev.* **2017**, *46*, 7176−7190.
(3) Greco, A.; Jiang, X.; Cao, D. An Investigation of Lithium-Ion Battery Thermal Management Using Paraffin/Porous-Graphite-Matrix Composite. *J. Power Sources* **2015**, *278*, 50−68.
(4) Li, J.; Li, J.; Luo, J. Superlubricity of Graphite Sliding against Graphene Nanoflake under Ultrahigh Contact Pressure. *Adv. Sci.* **2018**, *5*, No. 1800810.
(5) Gallego, N. C.; Klett, J. W. Carbon Foams for Thermal Management. *Carbon* **2003**, *41*, 1461−1466.
(6) Peng, J.; Chen, N.; He, R.; Wang, Z.; Dai, S.; Jin, X. Electrochemically Driven Transformation of Amorphous Carbons to Crystalline Graphite Nanoflakes: A Facile and Mild Graphitization Method. *Angew. Chem.* **2017**, *129*, 1777−1781.
(7) Deng, X.; Shi, W.; Zhong, Y.; Zhou, W.; Liu, M.; Shao, Z. Facile Strategy to Low-Cost Synthesis of Hierarchically Porous, Active Carbon of High Graphitization for Energy Storage. *ACS Appl. Mater. Interfaces* **2018**, *10*, 21573−21581.
(8) Thambiliyagodage, C. J.; Hakat, Y.; Bakker, M. G. One Pot Synthesis of Carbon/Ni Nanoparticle Monolithic Composites by Nanocasting and Their Catalytic Activity for 4-Nitrophenol Reduction. *Curr. Catal.* **2006**, *5*, 135−146.
(9) Rastegar, H.; Bavand-vandchali, M.; Nemati, A.; Golestani-Fard, F. Catalytic Graphitization Behavior of Phenolic Resins by Addition of in Situ Formed Nano-Fe Particles. *Phys. E* **2018**, *101*, 50−61.
(10) Lu, A.-H.; Li, W.-C.; Hao, G.-P.; Spliethoff, B.; Bongard, H.-J.; Schaack, B. B.; Schüth, F. Easy Synthesis of Hollow Polymer, Carbon, and Graphitized Microspheres. *Angew. Chem.* **2010**, *122*, 1659−1662.
(11) Aikawa, S.; Kizu, T.; Nishikawa, E. Catalytic Graphitization of an Amorphous Carbon Film under Focused Electron Beam Irradiation Due to the Presence of Sputtered Nickel Metal Particles. *Carbon* **2010**, *48*, 2997−2999.
(12) Thambiliyagodage, C.; Usgodaarachchi, L. Efficient Removal of Methylene Blue by Turbostratic Carbon/$Fe_3C$/Fe Composite Synthesized by Catalytic Graphitization of Sucrose. *Mater. Today Proc.* **2022**, *56*, 2189−2194.
(13) Hoekstra, J.; Beale, A. M.; Soulimani, F.; Versluijs-Helder, M.; Geus, J. W.; Jenneskens, L. W. Base Metal Catalyzed Graphitization of Cellulose: A Combined Raman Spectroscopy, Temperature-Dependent X-Ray Diffraction and High-Resolution Transmission Electron Microscopy Study. *J. Phys. Chem. C* **2015**, *119*, 10653−10661.
(14) Ōya, A.; Otani, S. Catalytic Graphitization of Carbons by Various Metals. *Carbon* **1979**, *17*, 131−137.
(15) Thambiliyagodage, C. J.; Ulrich, S.; Araujo, P. T.; Bakker, M. G. Catalytic Graphitization in Nanocast Carbon Monoliths by Iron, Cobalt and Nickel Nanoparticles. *Carbon* **2018**, *134*, 452−463.
(16) Thambiliyagodage, C.; Wijesekera, R.; Bakker, M. G. Leaching of Ilmenite to Produce Titanium Based Materials: A Review. *Discovery Mater.* **2021**, *1*, 1−28.
(17) Thambiliyagodage, C.; Wijesekera, R. Ball Milling—A Green and Sustainable Technique for the Preparation of Titanium Based Materials from Ilmenite. *Curr. Res. Green Sustainable Chem.* **2022**, *5*, No. 100236.
(18) Thambiliyagodage, C.; Mirihana, S.; Wijesekera, R.; Madusanka, D. S.; Kandanapitiye, M.; Bakker, M. Fabrication of $Fe_2TiO_5/TiO_2$ Binary Nanocomposite from Natural Ilmenite and Their Photocatalytic Activity under Solar Energy. *Curr. Res. Green Sustainable Chem.* **2021**, *4*, No. 100156.
(19) Charitha, T.; Leshan, U.; Shanitha, M.; Ramanee, W.; Buddi, L.; Martin, B. Efficient Photodegradation Activity of $\alpha$-$Fe_2O_3/Fe_2TiO_5/TiO_2$ and $Fe_2TiO_5/TiO_2$ Nanocomposites Synthesized from Natural Ilmenite. *Results Mater.* **2021**, *12*, No. 100219.
(20) Katheresan, V.; Kansedo, J.; Lau, S. Y. Efficiency of Various Recent Wastewater Dye Removal Methods: A Review. *J. Environ. Chem. Eng.* **2018**, *6*, 4676−4697.
(21) Saleh, I. A.; Zouari, N.; Al-Ghouti, M. A. Removal of Pesticides from Water and Wastewater: Chemical, Physical and Biological Treatment Approaches. *Environ. Technol. Innov.* **2020**, *19*, No. 101026.
(22) Santos, L. M.; Machado, W. A.; França, M. D.; Borges, K. A.; Paniago, R. M.; Patrocinio, A. O. T.; Machado, A. E. H. Structural Characterization of Ag-Doped $TiO_2$ with Enhanced Photocatalytic Activity. *RSC Adv.* **2015**, *5*, 103752−103759.
(23) Qasem, N. A. A.; Mohammed, R. H.; Lawal, D. U. Removal of Heavy Metal Ions from Wastewater: A Comprehensive and Critical Review. *npj Clean Water* **2021**, *4*, No. 36.
(24) Gracia-Lor, E.; Sancho, J. V.; Serrano, R.; Hernández, F. Occurrence and Removal of Pharmaceuticals in Wastewater Treatment Plants at the Spanish Mediterranean Area of Valencia. *Chemosphere* **2012**, *87*, 453−462.
(25) Shindhal, T.; Rakholiya, P.; Varjani, S.; Pandey, A.; Ngo, H. H.; Guo, W.; Ng, H. Y.; Taherzadeh, M. J. A Critical Review on Advances in the Practices and Perspectives for the Treatment of Dye Industry Wastewater. *Bioengineered* **2021**, *12*, 70−87.
(26) Przystaś, W.; Zablocka-Godlewska, E.; Grabinska-Sota, E. Biological Removal of Azo and Triphenylmethane Dyes and Toxicity of Process By-Products. *Water, Air, Soil Pollut.* **2012**, *223*, 1581−1592.
(27) dos Santos, A. B.; Cervantes, F. J.; van Lier, J. B. Review Paper on Current Technologies for Decolourisation of Textile Wastewaters: Perspectives for Anaerobic Biotechnology. *Bioresour. Technol.* **2007**, *98*, 2369−2385.
(28) Drumond Chequer, F. M.; Oliveira, G. A. R.; de Ferraz, E. R. A.; Cardoso, J. C.; Zanoni, M. V. B.; de Oliveira, D. P. Textile Dyes: Dyeing Process and Environmental Impact. *Eco-Friendly Text. Dyeing Finish.* **2013**, *6*, 151−176.
(29) Berradi, M.; Hsissou, R.; Khudhair, M.; Assouag, M.; Cherkaoui, O.; El Bachiri, A.; El Harfi, A. Textile Finishing Dyes and Their Impact on Aquatic Environs. *Heliyon* **2019**, *5*, No. e02711.
(30) Sharma, K. P.; Sharma, S.; Sharma, S.; Singh, P. K.; Kumar, S.; Grover, R.; Sharma, P. K. A Comparative Study on Characterization of Textile Wastewaters (Untreated and Treated) Toxicity by Chemical and Biological Tests. *Chemosphere* **2007**, *69*, 48−54.
(31) Usgodaarachchi, L.; Thambiliyagodage, C.; Wijesekera, R.; Bakker, M. G. Synthesis of Mesoporous Silica Nanoparticles Derived from Rice Husk and Surface-Controlled Amine Functionalization for Efficient Adsorption of Methylene Blue from Aqueous Solution. *Curr. Res. Green Sustainable Chem.* **2021**, *4*, No. 100116.
(32) Thambiliyagodage, C.; Ranchagoda, S.; Mirihana, S. A Comparison Study of Removing Rhodamine B from Wastewater by Nitric Acid Functionalized Rice Husk, Coconut Husk and Synthetic Porous Carbon. In *ICSBE 2020*, Dissanayake, R.; Mendis, P.; Weerasekera, K.; De Silva, S.; Fernando, S., Eds.; Springer: Singapore, 2022; Vol. *174*, pp 587−602.
(33) Thambiliyagodage, C. J.; Cooray, V. Y.; Perera, I. N.; Wijesekera, R. D. Eco-Friendly Porous Carbon Materials for Wastewater Treatment. *Lect. Notes Civ. Eng.* **2020**, *44*, 252−260.
(34) David, P. S.; Karunanithi, A.; Fathima, N. N. Improved Filtration for Dye Removal Using Keratin−Polyamide Blend Nanofibrous Membranes. *Environ. Sci. Pollut. Res.* **2020**, *27*, 45629−45638.
(35) Huang, R.; Zhang, Q.; Yao, H.; Lu, X.; Zhou, Q.; Yan, D. Ion-Exchange Resins for Efficient Removal of Colorants in Bis-(Hydroxyethyl) Terephthalate. *ACS Omega* **2021**, *6*, 12351−12360.
(36) Gadekar, M. R.; Ahammed, M. M. Coagulation/Flocculation Process for Dye Removal Using Water Treatment Residuals: Modelling through Artificial Neural Networks. *Desalin. Water Treat.* **2016**, *57*, 26392−26400.
(37) Thambiliyagodage, C.; Mirihana, S. Photocatalytic Activity of Fe and Cu Co-Doped $TiO_2$ Nanoparticles under Visible Light. *J. Sol-Gel Sci. Technol.* **2021**, *99*, 109−121.
(38) Geng, S.; Tian, F.; Li, M.; Liu, Y.; Sheng, J.; Yang, W.; Yu, Y.; Hou, Y. Activating Interfacial S Sites of $MoS_2$ Boosts Hydrogen Evolution Electrocatalysis. *Nano Res.* **2022**, *15*, 1809−1816.
(39) Zhang, X.; Tian, F.; Gao, M.; Yang, W.; Yu, Y. L-Cysteine Capped $Mo_2C/Zn_{0.67}Cd_{0.33}S$ Heterojunction with Intimate Covalent Bonds


https://doi.org/10.1021/acsomega.2c02336
*ACS Omega* 2022, 7, 25403−25421

Enables Efficient and Stable $H_2$-Releasing Photocatalysis. *Chem. Eng. J.* **2022**, *428*, No. 132628.
(40) Dong, G.; Chen, B.; Liu, B.; Hounjet, L. J.; Cao, Y.; Stoyanov, S. R.; Yang, M.; Zhang, B. Advanced Oxidation Processes in Micro-reactors for Water and Wastewater Treatment: Development, Challenges, and Opportunities. *Water Res.* **2022**, *211*, No. 118047.
(41) Ghernaout, D.; Elboughdiri, N.; Ghernaout, D.; Elboughdiri, N. Advanced Oxidation Processes for Wastewater Treatment: Facts and Future Trends. *Open Access Libr. J.* **2020**, *7*, 1−15.
(42) Mutuma, B. K.; Shao, G. N.; Kim, W. D.; Kim, H. T. Sol−Gel Synthesis of Mesoporous Anatase−Brookite and Anatase−Brookite−Rutile $TiO_2$ Nanoparticles and Their Photocatalytic Properties. *J. Colloid Interface Sci.* **2015**, *442*, 1−7.
(43) Zhao, D.; Yang, X.; Chen, C.; Wang, X. Enhanced Photocatalytic Degradation of Methylene Blue on Multiwalled Carbon Nanotubes−$TiO_2$. *J. Colloid Interface Sci.* **2013**, *398*, 234−239.
(44) Liao, Y.; Pan, K.; Wang, L.; Pan, Q.; Zhou, W.; Miao, X.; Jiang, B.; Tian, C.; Tian, G.; Wang, G.; Fu, H. Facile Synthesis of High-Crystallinity Graphitic Carbon/$Fe_3C$ Nanocomposites as Counter Electrodes for High-Efficiency Dye-Sensitized Solar Cells. *ACS Appl. Mater. Interfaces* **2013**, *5*, 3663−3670.
(45) Lv, T.; Pan, L.; Liu, X.; Sun, Z. Enhanced Photocatalytic Degradation of Methylene Blue by ZnO−Reduced Graphene Oxide−Carbon Nanotube Composites Synthesized via Microwave-Assisted Reaction. *Catal. Sci. Technol.* **2012**, *2*, 2297−2301.
(46) Kumbhakar, P.; Pramanik, A.; Biswas, S.; Kole, A. K.; Sarkar, R.; Kumbhakar, P. In-Situ Synthesis of RGO-ZnO Nanocomposite for Demonstration of Sunlight Driven Enhanced Photocatalytic and Self-Cleaning of Organic Dyes and Tea Stains of Cotton Fabrics. *J. Hazard. Mater.* **2018**, *360*, 193−203.
(47) Kumbhakar, P.; Biswas, S.; Kumbhakar, P. Observation of High Photocatalytic Activity by Tuning of Defects in Chemically Synthesized Ethylene Glycol Capped ZnO Nanorods. *Optik* **2018**, *154*, 303−314.
(48) Bao, S.; Wang, Y.; Wei, Z.; Yang, W.; Yu, Y. Highly Efficient Recovery of Heavy Rare Earth Elements by Using an Amino-Functionalized Magnetic Graphene Oxide with Acid and Base Resistance. *J. Hazard. Mater.* **2022**, *424*, No. 127370.
(49) Zhou, Q.; Chen, W.; Jiang, X.; Liu, H.; Ma, S.; Wang, B. Preparation of a Novel Nitrogen-Containing Graphitic Mesoporous Carbon for the Removal of Acid Red 88. *Sci. Rep.* **2020**, *10*, No. 1353.
(50) Cai, J.; Hu, S.; Xiang, J.; Zhang, H.; Men, D. The Effect of Graphitized Carbon on the Adsorption and Photocatalytic Degradation of Methylene Blue over $TiO_2$/C Composites. *RSC Adv.* **2020**, *10*, 40830−40842.
(51) Kuila, S. K.; Sarkar, R.; Kumbhakar, P.; Kumbhakar, P.; Tiwary, C. S.; Kundu, T. K. Photocatalytic Dye Degradation under Sunlight Irradiation Using Cerium Ion Adsorbed Two-Dimensional Graphitic Carbon Nitride. *J. Environ. Chem. Eng.* **2020**, *8*, No. 103942.
(52) Zhang, X.; Yang, W.; Gao, M.; Liu, H.; Li, K.; Yu, Y. Room-Temperature Solid Phase Surface Engineering of BiOI Sheets Stacking g-$C_3N_4$ Boosts Photocatalytic Reduction of Cr(VI). *Green Energy Environ.* **2022**, *7*, 66−74.
(53) Zhang, X.; Tian, F.; Lan, X.; Liu, Y.; Yang, W.; Zhang, J.; Yu, Y. Building P-Doped $MoS_2$/g-$C_3N_4$ Layered Heterojunction with a Dual-Internal Electric Field for Efficient Photocatalytic Sterilization. *Chem. Eng. J.* **2022**, *429*, No. 132588.
(54) Fouad, D. E.; Zhang, C.; El-Didamony, H.; Yingnan, L.; Mekuria, T. D.; Shah, A. H. Improved Size, Morphology and Crystallinity of Hematite ($\alpha$-$Fe_2O_3$) Nanoparticles Synthesized via the Precipitation Route Using Ferric Sulfate Precursor. *Results Phys.* **2019**, *12*, 1253−1261.
(55) Chen, X.; Wang, X.; Fang, D. A Review on C1s XPS-Spectra for Some Kinds of Carbon Materials. *Fullerenes, Nanotubes, Carbon Nanostruct.* **2020**, *28*, 1048−1058.
(56) Biesinger, M. C.; Payne, B. P.; Grosvenor, A. P.; Lau, L. W. M.; Gerson, A. R.; Smart, R. S. C. Resolving Surface Chemical States in XPS Analysis of First Row Transition Metals, Oxides and Hydroxides: Cr, Mn, Fe, Co and Ni. *Appl. Surf. Sci.* **2011**, *257*, 2717−2730.
(57) Biesinger, M. C.; Lau, L. W. M.; Gerson, A. R.; Smart, R. S. C. Resolving Surface Chemical States in XPS Analysis of First Row Transition Metals, Oxides and Hydroxides: Sc, Ti, V, Cu and Zn. *Appl. Surf. Sci.* **2010**, *257*, 887−898.
(58) Makuła, P.; Pacia, M.; Macyk, W. How To Correctly Determine the Band Gap Energy of Modified Semiconductor Photocatalysts Based on UV−Vis Spectra. *J. Phys. Chem. Lett.* **2018**, *9*, 6814−6817.
(59) Zhang, D.; Dong, S. Challenges in Band Alignment between Semiconducting Materials: A Case of Rutile and Anatase $TiO_2$. *Prog. Nat. Sci.: Mater. Int.* **2019**, *29*, 277−284.
(60) Singh, M.; Goyal, M.; Devlal, K. Size and Shape Effects on the Band Gap of Semiconductor Compound Nanomaterials. *J. Taibah Univ. Sci.* **2018**, *12*, 470−475.
(61) Shah, I.; Adnan, R.; Ngah, W. S. W.; Mohamed, N. Iron Impregnated Activated Carbon as an Efficient Adsorbent for the Removal of Methylene Blue: Regeneration and Kinetics Studies. *PLoS One* **2015**, *10*, No. e0122603.
(62) El Saliby, I.; Erdei, L.; Kim, J. H.; Shon, H. K. Adsorption and Photocatalytic Degradation of Methylene Blue over Hydrogen−Titanate Nanofibres Produced by a Peroxide Method. *Water Res.* **2013**, *47*, 4115−4125.
(63) Wang, X.; Zhang, P.; Wang, W.; Lei, X.; Zou, B.; Yang, H. Synthesis, Structure and Magnetic Properties of Graphite Carbon Encapsulated $Fe_3C$ Nanoparticles for Applications as Adsorbents. *RSC Adv.* **2015**, *5*, 27857−27861.
(64) Simonetti, E. A. N.; De Simone Cividanes, L.; Campos, T. M. B.; De Menezes, B. R. C.; Brito, F. S.; Thim, G. P. Carbon and $TiO_2$ Synergistic Effect on Methylene Blue Adsorption. *Mater. Chem. Phys.* **2016**, *177*, 330−338.
(65) Wu, F.; Liu, W.; Qiu, J.; Li, J.; Zhou, W.; Fang, Y.; Zhang, S.; Li, X. Enhanced Photocatalytic Degradation and Adsorption of Methylene Blue via $TiO_2$ Nanocrystals Supported on Graphene-like Bamboo Charcoal. *Appl. Surf. Sci.* **2015**, *358*, 425−435.
(66) Hristovski, K. D.; Markovski, J. Engineering Metal (Hydr)Oxide Sorbents for Removal of Arsenate and Similar Weak-Acid Oxyanion Contaminants: A Critical Review with Emphasis on Factors Governing Sorption Processes. *Sci. Total Environ.* **2017**, *598*, 258−271.
(67) Sarma, G. K.; Sen Gupta, S.; Bhattacharyya, K. G. Nanomaterials as Versatile Adsorbents for Heavy Metal Ions in Water: A Review. *Environ. Sci. Pollut. Res.* **2019**, *26*, 6245−6278.
(68) Sahoo, T. R.; Prelot, B. Adsorption Processes for the Removal of Contaminants from Wastewater. In *Nanomaterials for the Detection and Removal of Wastewater Pollutants: Micro and Nano Technologies*; Elsevier, 2020; pp 161−222. DOI: 10.1016/b978-0-12-818489-9.00007-4.
(69) Houas, A.; Lachheb, H.; Ksibi, M.; Elaloui, E.; Guillard, C.; Herrmann, J. M. Photocatalytic Degradation Pathway of Methylene Blue in Water. *Appl. Catal., B* **2001**, *31*, 145−157.
(70) Li, T.; Feng, C.; Yap, B. K.; Zhu, X.; Xiong, B.; He, Z.; Wong, W. Y. Accelerating Charge Transfer via Nonconjugated Polyelectrolyte Interlayers toward Efficient Versatile Photoredox Catalysis. *Commun. Chem.* **2021**, *4*, No. 150.
(71) Liu, H.; Li, Y.; Yuan, M.; Sun, G.; Liao, Q.; Zhang, Y. Solid and Macroporous Fe3C/N-C Nanofibers with Enhanced Electromagnetic Wave Absorbability. *Sci. Rep.* **2018**, *8*, No. 16832.